

CANADIAN THESES ON MICROFICHE

I.S.B.N.

THESES CANADIENNES SUR MICROFICHE



National Library of Canada
Collections Development Branch

Canadian Theses on
Microfiche Service

Ottawa, Canada
K1A 0N4

Bibliothèque nationale du Canada
Direction du développement des collections

Service des thèses canadiennes
sur microfiche

NOTICE

The quality of this microfiche is heavily dependent upon the quality of the original thesis submitted for microfilming. Every effort has been made to ensure the highest quality of reproduction possible.

If pages are missing, contact the university which granted the degree.

Some pages may have indistinct print especially if the original pages were typed with a poor typewriter ribbon or if the university sent us a poor photocopy.

Previously copyrighted materials (journal articles, published tests, etc.) are not filmed.

Reproduction in full or in part of this film is governed by the Canadian Copyright Act, R.S.C. 1970, c. C-30. Please read the authorization forms which accompany this thesis.

**THIS DISSERTATION
HAS BEEN MICROFILMED
EXACTLY AS RECEIVED**

AVIS

La qualité de cette microfiche dépend grandement de la qualité de la thèse soumise au microfilmage. Nous avons tout fait pour assurer une qualité supérieure de reproduction.

S'il manque des pages, veuillez communiquer avec l'université qui a conféré le grade.

La qualité d'impression de certaines pages peut laisser à désirer, surtout si les pages originales ont été dactylographiées à l'aide d'un ruban usé ou si l'université nous a fait parvenir une photocopie de mauvaise qualité.

Les documents qui font déjà l'objet d'un droit d'auteur (articles de revue, examens publiés, etc.) ne sont pas microfilmés.

La reproduction, même partielle, de ce microfilm est soumise à la Loi canadienne sur le droit d'auteur, SRC 1970, c. C-30. Veuillez prendre connaissance des formules d'autorisation qui accompagnent cette thèse.

**LA THÈSE A ÉTÉ
MICROFILMÉE TELLE QUE
NOUS L'AVONS REÇUE**



National Library
of Canada

Bibliothèque nationale
du Canada

Canadian Theses Division / Division des thèses canadiennes

Ottawa, Canada
K1A 0N4

54060

0-315-06140-5

PERMISSION TO MICROFILM — AUTORISATION DE MICROFILMER

• Please print or type — Écrire en lettres moulées ou dactylographier

Full Name of Author — Nom complet de l'auteur

SRIPEN TOWTA

Date of Birth — Date de naissance

27, 1 / 49

Country of Birth — Lieu de naissance

THAILAND

Permanent Address — Résidence fixe

Dept. of Physics, Chiang Mai University
Chiang Mai THAILAND

Title of Thesis — Titre de la thèse

ORIENTATION DEPENDENCE OF THE NUCLEAR QUADRUPOLE
SPIN-LATTICE RELAXATION IN CRYSTALS

University — Université

U. of Alberta

Degree for which thesis was presented — Grade pour lequel cette thèse fut présentée

M.Sc

Year this degree conferred — Année d'obtention de ce grade

1981

Name of Supervisor — Nom du directeur de thèse

D. G. Hughes

Permission is hereby granted to the NATIONAL LIBRARY OF CANADA to microfilm this thesis and to lend or sell copies of the film.

The author reserves other publication rights, and neither the thesis nor extensive extracts from it may be printed or otherwise reproduced without the author's written permission

L'autorisation est, par la présente, accordée à la BIBLIOTHÈQUE NATIONALE DU CANADA de microfilmer cette thèse et de prêter ou de vendre des exemplaires du film.

L'auteur se réserve les autres droits de publication, ni la thèse ni de longs extraits de celle-ci ne doivent être imprimés ou autrement reproduits sans l'autorisation écrite de l'auteur

Date

Sept 30, 1981

Signature

S Towta

THE UNIVERSITY OF ALBERTA

ORIENTATION DEPENDENCE OF THE NUCLEAR QUADRUPOLE
SPIN-LATTICE RELAXATION TIME IN CRYSTALS

by



Sripen Towta

A THESIS

SUBMITTED TO THE FACULTY OF GRADUATE STUDIES AND RESEARCH
IN PARTIAL FULFILMENT OF THE REQUIREMENTS FOR THE DEGREE
OF MASTER OF SCIENCE

DEPARTMENT OF PHYSICS

EDMONTON, ALBERTA

FALL, 1981

THE UNIVERSITY OF ALBERTA

RELEASE FORM

NAME OF AUTHOR . . . Sripen Towta
TITLE OF THESIS . . . Orientation Dependence of the Nuclear
Quadrupole Spin-Lattice Relaxation Time
in Crystals
DEGREE FOR WHICH THESIS WAS PRESENTED . . . M. Sc.
YEAR THIS DEGREE GRANTED . . . 1981

Permission is hereby granted to THE UNIVERSITY OF ALBERTA LIBRARY to reproduce single copies of this thesis and to lend or sell such copies for private, scholarly or scientific research purposes only.

The author reserves other publication rights, and neither the thesis nor extensive extracts from it may be printed or otherwise reproduced without the author's written permission.

(Signed) . . . S. Towta

PERMANENT ADDRESS:

Department of Physics
Chiang Mai University
Chiang Mai, Thailand

DATED . *Sept 21,* . 1981

THE UNIVERSITY OF ALBERTA
FACULTY OF GRADUATE STUDIES AND RESEARCH

The undersigned certify that they have read, and
recommend to the Faculty of Graduate Studies and Research,
for acceptance, a thesis entitled .Orientation.
Dependence of the Nuclear Quadrupole Spin-Lattice
Relaxation Time in Crystals.
submitted by . Sripen Towta.
in partial fulfilment of the requirements for the
degree of Master of Science.

D. G. Hill
Supervisor

Robert E. Jordan

A. B. Bhalerao

P. S. Steiner

Date *September 21, 1981*

ABSTRACT

In this thesis we describe a pulsed NMR spectrometer suitable for work on solids. A novel feature is a simple tapped-coil arrangement that enables an impedance match to be obtained between the NMR tuned circuit and the equipment feeding it. Also we describe a sample holder that enables the orientation of single crystals within the NMR coil to be varied about two perpendicular axes.

The spin-lattice relaxation time T_1 of ^{23}Na in doped saturated aqueous solution of NaNO_3 and in a single crystal of NaCl were measured in order to study the behaviour of the spectrometer. The T_1 of ^{23}Na in the doped saturated aqueous solution of NaNO_3 was found to be 20.4 ms, in rough agreement with a crude theoretical estimate. The T_1 of ^{23}Na in NaCl at 299K was found to be 14.6 ± 0.15 s. This is in only fair agreement with other published values.

Finally, the orientation dependence of the T_1 of ^{23}Na in a single crystal of NaNO_3 was measured. It was found to be independent of crystal orientation, as predicted theoretically. Also, the T_1 value of 6.19 s at 299K is in excellent agreement with values found by other workers. However, such excellent agreement is fortuitous, since recent measurements with our equipment have shown that different values of T_1 are obtained, depending on the control settings of the rf phase-sensitive detector.

ACKNOWLEDGEMENTS

I wish to express my sincere gratitude to Dr. D.G. Hughes, my research supervisor, for his continual help, interest and encouragement throughout the work.

I also wish to thank Dr. L. Pandey for several helpful discussions and for assistance with the equipment.

I am grateful to Mr. Earl Cairns, Mr. Ed Reid and Mr. Willy Siewert for the design, construction and repair of the electronic equipment. Thanks also to the late Mr. Nick Riebeek and Mr. Gilbert LaChat for the construction of the NMR probe and sample holder.

It is a pleasure to acknowledge financial support from the University of Alberta in the form of a Graduate Assistantship.

Finally, I would like to thank Mrs. Ruth Nelson for typing this thesis.

TABLE OF CONTENTS

	Page
CHAPTER 1 INTRODUCTION	1
CHAPTER 2 THEORY	6
2.1 Description of NMR.	6
2.1.1 Energy level description.	6
2.1.2 Pulsed NMR.	8
2.2 Nuclear quadrupole interaction.	18
2.3 Orientation dependence of the nuclear quadrupole spin-lattice relaxation in crystals.	28
CHAPTER 3 EXPERIMENTAL DETAILS AND RESULTS	27
3.1 Apparatus	37
3.1.1 Brief description of the pulsed NMR spectrometer.	37
3.1.2 Sample probe.	40
3.1.3 Lumped circuit duplexer.	44
3.1.4 R.F. phase-sensitive detector.	46
3.1.5 R.F. gated amplifier	47
3.1.6 Signal averager	47
3.1.7 Pulse generator	48
3.2 Details of sample.	52
3.2.1 Description of the sodium nitrate crystal.	52

	Page
3.2.2 Crystallography of NaNO_3 .	52
3.3 Preliminary check of the equipment.	55
3.4 Measurement of the spin-lattice relaxation time T_1 of ^{23}Na , in sodium chloride.	64
3.5 Measurement of the orientation dependence of the spin-lattice relaxation time of ^{23}Na in NaNO_3 .	70
3.5.1 Installation of the NaNO_3 crystal in the sample holder.	70
3.5.2 Choice of crystal coordinate system for NaNO_3 .	73
3.5.3 Measurement of T_1 of ^{23}Na in NaNO_3 .	75
 CHAPTER 4 DISCUSSION	 82
 BIBLIOGRAPHY	 90
 APPENDIX 1 Weighted least squares fit to a straight line and the error in the fitted parameters.	 93
 APPENDIX 2 Method of obtaining the standard deviations and weighting factors needed in our least squares fitting procedure.	 97

APPENDIX 3 Program for calculating T_1 from
values of $(\bar{M}_0 - M_2)$ and τ .

LIST OF TABLES

Table		Page
1	<p>T_1 of ^{23}Na in NaCl obtained using data from different channels of the signal averager.</p>	69
2	<p>T_1 of ^{23}Na in NaNO_3 at $\theta = 54.7^\circ$ and at various values of ϕ. The values in the second, third, fourth and fifth columns were obtained using data from different channels of the signal averager.</p>	81

LIST OF FIGURES

Figure		Page
2.1	Precession of the nuclear magnetization in the rotating coordinate system.	13
2.2	Schematic representation of (a) the FID following a 90° pulse, (b) the FID following a 180° - τ - 90° pulse sequence.	16
2.3	Orientation of the external magnetic field relative to the principal axes of the crystal.	25
2.4	Nuclear electric quadrupole transitions for $I = 3/2$.	31
3.1	Block diagram of the system.	39
3.2	Circuit diagram of the sample probe and the lumped circuit duplexer.	42
3.3	Schematic diagram of the pulse generator. The arrows indicate the direction of information flow.	50
3.4	Unit cell of sodium nitrate.	54
3.5	$M_0 - M_z$ versus pulse separation time τ for ^{23}Na in a doped saturated aqueous solution of NaNO_3 at 299K.	62
3.6	$\bar{M}_0 - M_z$ versus pulse separation time τ for ^{23}Na in NaCl at 299K.	67
3.7	Diagram of the sample holder.	72
3.8	Free induction decay $F(t)$ of ^{23}Na in NaNO_3 at $\theta = 54.7^\circ$, and $\phi = 0^\circ$ and 60° .	77

Figure

Page

- 3.9 $\bar{M}_O - M_Z$ versus pulse separation time τ for ^{23}Na in NaNO_3 at 299K and $\phi = 30^\circ$ 80
- 4.1 T_1 of ^{23}Na in a single crystal of NaNO_3 at 299K, as a function of ϕ for $\theta = 54.7^\circ$ 87

CHAPTER 1

INTRODUCTION

Nuclei with spin number $I \geq 1$ possess an electric quadrupole moment in addition to a magnetic dipole moment. It has been shown by Pound (1950) that the interaction of the nuclear electric quadrupole moment with the time-averaged electric field gradient at the nuclear site affects the shape of the NMR absorption signal. In the case of a single crystal, the interaction causes the NMR line to be split into several components. For a polycrystalline sample, it broadens the NMR line. Pound (1950) also showed that the interaction of the nuclear quadrupole moment with a time-dependent electric field gradient causes spin-lattice relaxation. The main contribution to the spin-lattice relaxation is caused by the fluctuating electric field gradient associated with phonons (Van Kranendonk, 1954; Wikner et al., 1960; Weber, 1963; Van Kranendonk and Walker, 1968). However, the fluctuating electric field gradient associated with the rotation of molecular or ionic groups and with the diffusion of charged defects (Cohen and Reif, 1957; Satoh, 1965; Becker, 1978) through the lattice also contribute significantly to spin-lattice relaxation in certain temperature ranges.

For nuclei such as ^{23}Na in NaCl which are situated at sites possessing cubic symmetry, the time-averaged electric field gradient is zero. The nuclear Zeeman levels are then equally spaced and only a single NMR line

is observed. Also, mutual spin flips or spin exchanges of the type $m, m' \rightarrow m \pm 1, m' \mp 1$ occur sufficiently rapidly to maintain a Boltzmann distribution among the nuclear Zeeman levels (Abragam and Proctor, 1958). In that case, the approach to equilibrium of M_z , the component of the nuclear magnetization along the external magnetic field direction, is exponential (Mieher, 1960; Zak, 1964), i.e. is of the form $M_z = (M_z)_0 (1 - e^{-t/T_1})$ where T_1 is the so-called spin-lattice relaxation time and $(M_z)_0$ is the equilibrium value of M_z . For nuclei situated at sites with lower than cubic symmetry, the spin-lattice relaxation is usually non-exponential. For example, for a spin system with $I = 3/2$, the approach to equilibrium is in general given by the sum of 3 exponentials (Andrew and Tunstall, 1961). The three relaxation times are $1/2W_1$, $1/2W_2$ and $1/2(W_1 + W_2)$, where W_1 and W_2 are the probabilities of $\Delta m = \pm 1$ and ± 2 transitions respectively (Yosida and Moriya, 1956).

Because of the non-exponential behaviour, experimental studies of the spin-lattice relaxation of nuclear spins in non-cubic single crystals are not easy to interpret. There is also the additional problem that it is difficult to selectively excite, by short rf pulses, individual NMR lines in multi-line spectra. Most measurements of the spin-lattice relaxation time in non-cubic single crystals have therefore been made with the crystal oriented relative to the external magnetic field so that the quadrupole splittings are essentially zero, i.e. so that all the

resonances overlap. When this is done, a Boltzmann distribution among the Zeeman energy levels is maintained by spin exchanges (Abragam and Proctor, 1958), just as in the case of a cubic crystal. The spin-lattice relaxation behaviour is then exponential, and is characterized by a single quadrupole relaxation time T_1 .

The orientation of an external magnetic field relative to a crystal has 2 degrees of freedom. The requirement of resonance overlap removes one of these degrees of freedom. The question can therefore be asked whether the quadrupole relaxation time T_1 is uniquely determined by the overlap condition or whether it varies with the remaining degree of freedom.

Bonera et al. (1970) and Avogadro et al. (1971) have measured the temperature dependence of the spin-lattice relaxation time of ^{23}Na in NaNO_2 . Kasahara et al. (1977) have measured the temperature dependence of the spin-lattice relaxation time of ^{23}Na in NaNO_3 . None of these workers specified the orientation of their crystal with respect to the external magnetic field, except to say that the crystal was set so that the resonances overlapped. It would seem that these workers believed that T_1 is uniquely determined by the resonance overlap condition.

Hughes and Spencer (1979) have shown that for certain types of relaxation processes, in particular the Raman-type two-phonon process, T_1 can be expressed as a linear combination of the components of a second-rank tensor,

subject of course to the constraint that resonance overlap occurs. It can then be shown that T_1 is independent of crystal orientation for nuclei situated at sites possessing tetragonal, trigonal, hexagonal, and cubic point-group symmetries. This is not the case for nuclei situated at sites possessing triclinic, monoclinic and orthorhombic point-group symmetries.

The ^{23}Na nuclei in NaNO_3 are situated at sites possessing trigonal symmetry. The spin-lattice relaxation time of these nuclei should therefore be uniquely determined by the resonance overlap condition, provided that the relaxation is caused by a Raman-type two-phonon process. The ^{23}Na nuclei in NaNO_2 are situated at sites possessing orthorhombic symmetry. Thus, irrespective of the type of relaxation mechanism involved, the T_1 of these nuclei is not uniquely determined by the resonance overlap condition.

The purpose of the work described in this thesis is to investigate the theoretical prediction of Hughes and Spencer (1979), in particular to confirm that T_1 for ^{23}Na in NaNO_3 is independent of crystal orientation. This spin system was chosen in preference to the more interesting case of ^{23}Na in NaNO_2 , because more complete resonance overlap can be achieved for ^{23}Na in NaNO_3 on account of the smaller second-order quadrupole shifts. In other words, the easier case was treated first.

Spin-lattice relaxation times were measured by the so-called 180° - τ - 90° pulse method. In this method, a

"180° pulse" is applied to the nuclear spin system. This reverses the direction of the nuclear magnetization. A "90° pulse" is applied to the spin system at a time τ later. This brings the nuclear magnetization into a transverse direction so that it precesses around the magnetic field and can then be detected as a rf voltage induced in the NMR coil. The amplitude of the NMR signal immediately following the 90° pulse is a measure of the value of M_z immediately before the pulse. The spin-lattice relaxation time T_1 is obtained from the τ dependence of the amplitude of the NMR signal.

The pulsed NMR spectrometer, which was built as part of this work, is described in the thesis. Also described is the method of data collection and analysis which avoids many types of systematic errors. Since this is the first time that pulsed NMR measurements have been made in this laboratory, some time was spent studying the behaviour, in particular the limitations, of the spectrometer. These also are described in this thesis.

CHAPTER 2

THEORY

2.1 Description of NMR

2.1.1 Energy level description

If a nucleus possessing a magnetic moment $\vec{\mu}$ and angular momentum $\hbar\vec{I}$ is placed in a steady magnetic field \vec{H}_0 directed along the z axis, the so-called Zeeman Hamiltonian describing the interaction can be written as

$$\mathcal{H} = -\vec{\mu} \cdot \vec{H}_0 \quad (2.1)$$

$$= -\gamma\hbar I_z H_0, \quad (2.2)$$

where I_z is the z component of the nuclear spin \vec{I} , and γ is the gyromagnetic ratio of the nucleus defined as,

$$\gamma = \vec{\mu} / \hbar\vec{I}. \quad (2.3)$$

The eigenvalues of the Hamiltonian are

$$E_m = -\gamma\hbar m H_0, \quad (2.4)$$

where m is the magnetic quantum number which may take any of the $2I+1$ values $I, I-1, \dots, -I$.

The energy levels of the nucleus are thus equally

spaced with the distance between adjacent ones being $\gamma\hbar H_0$. Transitions between adjacent levels can be induced by an oscillating magnetic field perpendicular to H_0 provided its frequency satisfies the equation

$$\hbar\omega_0 = \gamma\hbar H_0 \tag{2.5}$$

or

$$\omega_0 = \gamma H_0 \tag{2.6}$$

The frequency ω_0 is called the NMR frequency.

In thermal equilibrium, the lower energy levels are more highly populated than the upper ones, in accordance with the Boltzmann distribution. Since the probability of an upward transition between a pair of levels is the same as that of a downward transition between the same pair of levels, there will be a net absorption of energy by the nuclear spin system from an oscillating magnetic field satisfying the resonance condition. This absorption of energy will tend to equalize the populations of the energy levels, a phenomenon called saturation. However, the interaction between the nuclear spins and other degrees of freedom of the sample material, the so-called spin lattice interaction, will tend to restore thermal equilibrium. If a non-equilibrium situation is produced, by a resonant oscillating magnetic field for example, the population differences will, in the absence of the oscillating magnetic field, approach their equilibrium values exponen-

tially with a time constant called the spin-lattice relaxation time T_1 .

In practice, the Zeeman energy levels are not sharp, since they are broadened by nuclear magnetic dipole-dipole interactions and other interactions. By measuring the rf energy absorbed by the nuclear spin system as a function of frequency, the so-called absorption line shape $f(\omega)$ can be obtained. An expression for the mean square width or second moment of $f(\omega)$ caused by dipole-dipole interactions has been given by Van Vleck (1948).

In liquids, the dipole-dipole interactions are averaged out by molecular motions so that the absorption signals are intrinsically very narrow. In such cases, the observed width and shape of the absorption signal is often governed by the inhomogeneity of the external magnetic field H_0 .

2.1.2 Pulsed NMR

An alternative description is the following. The classical equation of motion for an object of magnetic moment $\vec{\mu}$ and angular momentum $h\vec{I}$, situated in a magnetic field \vec{H}_0 is

$$d\vec{\mu}/dt = \gamma\vec{\mu} \times \vec{H}_0 \quad (2.7)$$

It can be shown (Slichter, 1963) that the expectation value of the magnetic moment $\langle \vec{\mu} \rangle$ is given by a similar

equation, namely

$$d\langle\vec{\mu}\rangle/dt = \gamma\langle\vec{\mu}\rangle \times \vec{H}_0. \quad (2.8)$$

For a group of nuclei, the total magnetic moment or macroscopic magnetization is given by

$$\vec{M} = \sum \vec{\mu}_k \quad (2.9)$$

where $\vec{\mu}_k$ is the magnetic moment of the k th nucleus. If the nuclei are identical, the equation of motion for the macroscopic magnetization is

$$d\vec{M}/dt = \gamma\vec{M} \times \vec{H}_0. \quad (2.10)$$

It is convenient to view the motion of the magnetization from a frame of reference rotating about \vec{H}_0 with an angular velocity $\vec{\Omega}$. The equation of motion of the magnetization viewed from the rotating coordinate system is (Slichter, 1963)

$$d\vec{M}_{\text{rot}}/dt = \vec{M}_{\text{rot}} \times (\gamma\vec{H}_0 + \vec{\Omega}). \quad (2.11)$$

If $\vec{\Omega} = -\gamma\vec{H}_0$, then $d\vec{M}_{\text{rot}}/dt$ is zero and \vec{M}_{rot} is time independent. This shows that the nuclear magnetization precesses indefinitely around \vec{H}_0 at a frequency Ω which is numerically equal to ω_0 (see Eq. (2.6)). The frequency

Ω is called the Larmor frequency and is thus equal to the NMR frequency. The sense of the precession is governed by the sign γ .

Suppose a rotating magnetic field

$$\vec{H}_1 = H_1(\hat{i}\cos\omega t + \hat{j}\sin\omega t) \quad (2.12)$$

directed at right angles to \vec{H}_0 is applied to the spin system. Viewed from a coordinate system that rotates about the z axis at the same frequency ω as \vec{H}_1 , and with H_1 directed along the x axis, the equation of motion of the magnetization becomes

$$d\vec{M}_{\text{rot}}/dt = \vec{M}_{\text{rot}} \times [\hat{i}\gamma H_1 + \hat{k}(\omega + \gamma H_0)]. \quad (2.13)$$

In this rotating frame, the magnetization precesses about a static effective magnetic field

$$\vec{H}_{\text{eff}} = \hat{i}H_1 + \hat{k}(H_0 + \frac{\omega}{\gamma}). \quad (2.14)$$

At resonance, when $\omega = -\gamma H_0$, i.e. when ω is numerically equal to the NMR frequency ω_0 ,

$$\vec{H}_{\text{eff}} = \hat{i}H_1 \quad (2.15)$$

and the effective field is directed along the x axis of the rotating coordinate system. If the nuclear

magnetization is initially parallel to \vec{H}_0 , as it would be in thermal equilibrium for example, then the magnetization will precess in the yz plane about the x axis of the rotating frame with a frequency γH_1 . If the rotating magnetic field H_1 is applied for a short time τ_p say, the angle through which \vec{M} precesses in the rotating frame is given in radians by

$$\theta = \gamma H_1 \tau_p. \quad (2.16)$$

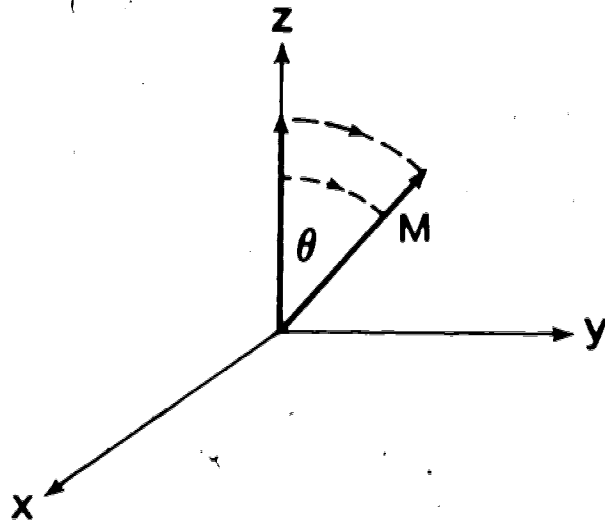
The situation is shown in Fig. 2.1 (a). Of particular importance are so-called 90° and 180° pulses whose lengths (or amplitudes) are chosen so as to turn the nuclear magnetization through 90° and 180° respectively in the rotating coordinate system. The effect of such pulses are shown in Figs. 2.1 (b) and (c).

Suppose a 180° pulse is applied to a spin system which was initially in thermal equilibrium. The pulse reverses the magnetization so that the z-component M_z is equal to $-M_0$, where M_0 is the value of the magnetization in thermal equilibrium. Because of the spin-lattice interaction, the nuclear magnetization will relax toward M_0 . For a spin system with $I = \frac{1}{2}$, the relaxation is always exponential and the time constant is called the longitudinal relaxation time or spin-lattice relaxation time T_1 . The time dependent magnetization following a 180° pulse at time $t = 0$ is therefore

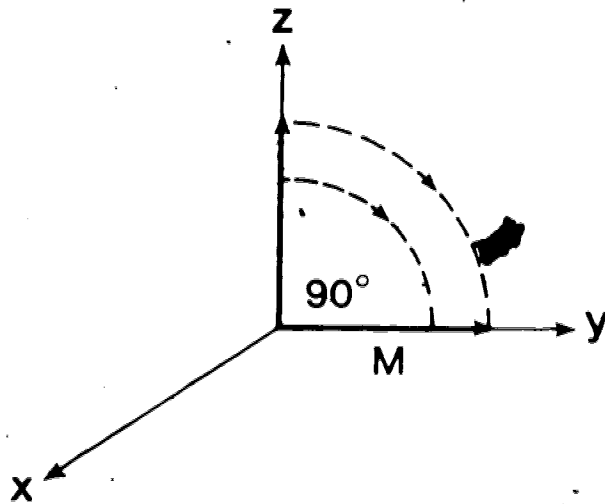
Figure 2.1

Precession of the nuclear magnetization (for $\gamma > 0$) about the x axis of the rotating coordinate system when a rf magnetic field H_1 is applied along the x axis for a short time τ_p . In case (a) $\gamma H_1 \tau_p = \theta$. Cases (b) and (c) show 90° and 180° pulses where $\gamma H_1 \tau_p = \pi/2$ and π respectively.

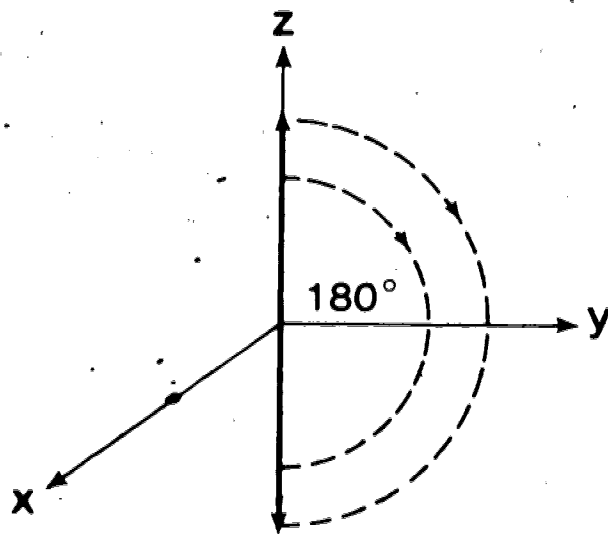
(a)



(b)



(c)

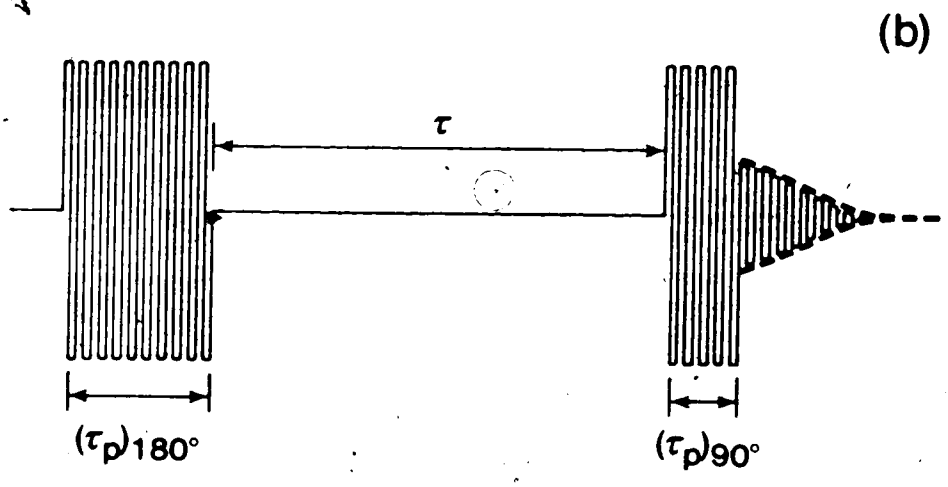
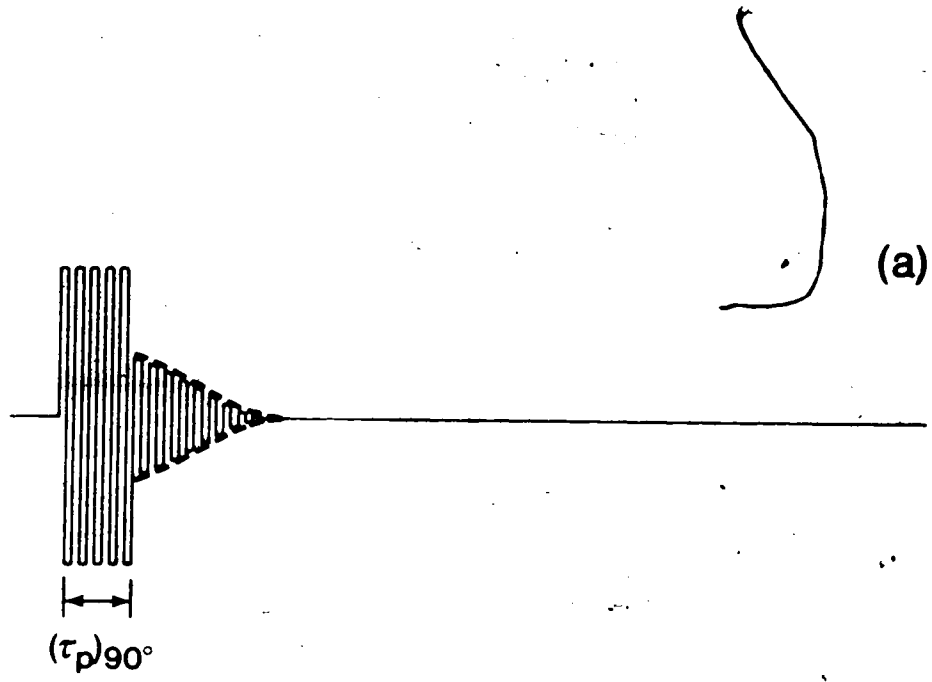


$$M_z = M_0 [1 - 2\exp(-t/T_1)]. \quad (2.17)$$

Suppose a 90° pulse is applied to a spin system which was initially in thermal equilibrium. Immediately after the pulse, the longitudinal or z-component of the magnetization is zero and we have a transverse component of magnetization M_0 which precesses around H_0 with an angular frequency ω_0 in the laboratory coordinate system. This precessing magnetization, with its associated time-dependent magnetic flux, induces a rf voltage in a coil wound around the sample. This voltage is the so-called NMR signal. Because of the magnetic dipole-dipole interaction between nuclear spins, the transverse magnetization decays toward its thermal equilibrium value of zero. The 90° pulse and the decaying NMR signal are shown schematically in Fig. 2.2 (a). The NMR signal, or more precisely its envelope, indicated by the dashed line in the figure, is called the free induction decay $F(t)$ say. It can be shown (Abragam, 1961) that $F(t)$ is the Fourier transform of the absorption line shape function $f(\omega)$ mentioned in the previous section. In some cases, especially liquids and gases, this decay is exponential and the time constant is called the spin-spin relaxation time T_2 . In solids, the spin-spin relaxation is usually non-exponential. However, an effective T_2 is often used to indicate the time scale of the decay of the transverse magnetization. In liquids and gases, the decay is often dominated by the

Figure 2.2

Schematic representation of (a) the FID following a 90° pulse, (b) the FID following a 180° - τ - 90° pulse sequence.



the inhomogeneity of the external magnetic field.

The spin-lattice relaxation time T_1 can be measured by performing an inversion recovery experiment in which a 180° pulse followed a time τ later by a 90° pulse is applied to the spin system. The 180° pulse reverses the z component of the magnetization. This then recovers toward its equilibrium value in accordance with Eq. (2.17). The z-component of magnetization, which is not directly observable by NMR, is made observable by applying a 90° pulse which rotates M_z into the transverse direction. The pulse and the free induction decay are shown schematically in Fig. 2.2 (b). A measurement of the amplitude of the FID immediately following the 90° pulse is a measure of M_z at a time τ after the 180° pulse. By rearranging Eq. (2.17), it can be shown that

$$\ln(M_0 - M_z) = \ln 2M_0 - \tau/T_1. \quad (2.18)$$

Thus by plotting $\ln(M_0 - M_z)$ as a function of τ , one can determine T_1 from the slope of a straight line graph.

It can then be noted that it is not essential for the magnetization to be perfectly reversed. If the 180° pulse is not perfect, M_z will still recover exponentially, according to an equation of the form

$$\ln(M_0 - M_z) = A - \tau/T_1. \quad (2.19)$$

Also, the 90° pulse need not be perfect, so long as $\tau > T_2$ which implies that $T_1 \gg T_2$. In many solids this is the case, so the measurements should be free from systematic errors caused by pulse imperfections.

2.2 Nuclear quadrupole interactions

For a nucleus which has a spin number $I \geq 1$, it is necessary to take into account the electrostatic interaction of the nucleus with its surroundings. The electrostatic Hamiltonian is

$$\mathcal{H} = \int \rho(\vec{r}) V(\vec{r}) dV \quad (2.20)$$

where $\rho(\vec{r})$ is the nuclear charge density, $V(\vec{r})$ is the electrostatic potential of the charges external to the nucleus and the integral is over the nuclear volume. By expressing the potential $V(\vec{r})$ in a Taylor expansion about the nuclear center of mass, the Hamiltonian becomes

$$\begin{aligned} \mathcal{H} &= \int \rho(\vec{r}) \left[V_0 + \sum_j \left(\frac{\partial V}{\partial x_j} \right)_0 x_j + \frac{1}{2} \sum_{jk} \left(\frac{\partial^2 V}{\partial x_j \partial x_k} \right)_0 x_j x_k + \dots \right] dV \\ &= ZeV_0 + \sum_j P_j \left(\frac{\partial V}{\partial x_j} \right)_0 + \frac{1}{2} \sum_{jk} Q_{jk} \left(\frac{\partial^2 V}{\partial x_j \partial x_k} \right)_0 + \dots \end{aligned} \quad (2.21)$$

where $\int \rho(\vec{r}) dV$ is Ze the nuclear charge,

$\int \rho(\vec{r}) x_j dV$ is P_j the nuclear electric dipole moment,

$\int \rho(\vec{r}) x_j x_k dV$ is Q'_{jk} the nuclear electric quadrupole moment tensor.

Since the first term in the Hamiltonian is orientation independent, it is omitted. Furthermore, because of parity considerations, the electric dipole moment (and the electric octapole moment etc.) relative to the nuclear center of mass vanishes. Thus, the expression for the Hamiltonian can be written as

$$\mathcal{H} = \frac{1}{2} \sum_{jk} Q'_{jk} V_{jk} + \text{hexadecapole term} + \dots \quad (2.22)$$

where $V_{jk} = \partial^2 V / \partial x_j \partial x_k$. The hexadecapole interaction is negligible in all practical cases (Abragam, 1961). Therefore we need only consider the quadrupole Hamiltonian

$$\mathcal{H}_Q = \frac{1}{2} \sum_{jk} Q'_{jk} V_{jk} \quad (2.23)$$

The quadrupole moment tensor Q'_{jk} is symmetric and thus has six independent components. It is convenient to define a simple tensor Q_{jk} which is both symmetric and traceless. This is done by writing

$$Q_{jk} = 3Q'_{jk} - \delta_{jk} \sum_e Q_{ee} \quad (2.24)$$

where δ_{jk} is the Kronecker delta function. By substituting Q'_{jk} from Eq. (2.24) in Eq. (2.23) and

ignoring the term involving traces since it is independent of the nuclear orientation, it is found that

$$\mathcal{H}_Q = \frac{1}{6} \sum_{jk} Q_{jk} V_{jk}. \quad (2.25)$$

By using the theorem that the corresponding matrix elements of all traceless, second-rank, symmetric tensors are proportional (Ramsey, 1953), it can be shown (Cohen and Reif, 1957) that the matrix elements of the quadrupole Hamiltonian are given by

$$\langle m' | \mathcal{H}_Q | m \rangle = [eQ/6I(2I-1)] \sum_{jk} \langle m' | \frac{3}{2} (I_j I_k + I_k I_j) - \delta_{jk} I^2 | m \rangle V_{jk} \quad (2.26)$$

where Q is a scalar quantity called the nuclear quadrupole moment and is defined as

$$eQ = \int \rho(\vec{r}) (3z^2 - r^2) dV \quad (2.27)$$

where $\rho(\vec{r})$ is the nuclear charge density and z is along the axis of the spin of the nucleus. By introducing the raising and lowering spin operators,

$$I_{\pm} = I_x \pm iI_y \quad (2.28)$$

the Hamiltonian becomes

$$\begin{aligned}
\langle m' | \mathcal{H} | m \rangle = & [eQ/4I(2I-1)] \langle m' | (3I_z^2 - I^2)V_0 + (I_+ I_z + I_z I_+)V_{-1} \\
& + (I_- I_z + I_z I_-)V_{+1} + I_+^2 V_{-2} + I_-^2 V_{+2} | m \rangle, \quad (2.29)
\end{aligned}$$

where

$$\left. \begin{aligned}
V_0 &= V_{zz} \\
V_{\pm 1} &= V_{xz} \pm iV_{yz} \\
V_{\pm 2} &= \frac{1}{2} (V_{xx} - V_{yy}) \pm iV_{xz}
\end{aligned} \right\} \quad (2.30)$$

In a representation that diagonalizes the Zeeman energy, the matrix elements of \mathcal{H}_Q are

$$\langle m | \mathcal{H}_Q | m \rangle = A[3m^2 - I(I+1)]V_0 \quad (2.31)$$

$$\langle m \pm 1 | \mathcal{H}_Q | m \rangle = A(2m \pm 1)[(I \mp m)(I \pm m + 1)]^{\frac{1}{2}} V_{\mp 1} \quad (2.32)$$

$$\langle m \pm 2 | \mathcal{H}_Q | m \rangle = A[(I \mp m)(I \mp m - 1)(I \pm m + 1)(I \pm m + 2)]^{\frac{1}{2}} V_{\mp 2} \quad (2.33)$$

$$\langle m' | \mathcal{H}_Q | m \rangle = 0 \quad \text{for} \quad |m' - m| > 2 \quad (2.34)$$

where $A = eQ/4I(2I-1)$.

In the so-called high field case, the quadrupole Hamiltonian is treated as a perturbation on the Zeeman energy. The Hamiltonian of the spin system is then given by

$$\mathcal{H} = -\gamma h m H_0 + \mathcal{H}_Q \quad (2.35)$$

where the matrix elements of \mathcal{H}_Q are given in Eqs. (2.31), (2.32), (2.33), (2.34).

The energy to the second order in the quadrupole interaction is (Bersohn, 1952)

$$E_m = -\gamma h m H_0 + A [3m^2 - I(I+1)] V_0 + 2A^2 \frac{(V_{+1})(V_{-1})}{\gamma h H_0} m \times \quad (2.36)$$

$$[4I(I+1) - 1 - 8m^2] - 2A^2 \frac{(V_2)(V_{-2})}{\gamma h H_0} m [2I(I+1) - 1 - 2m^2]$$

The NMR frequencies are governed by the time-averaged values of E_m and these values are in turn governed by the time-average values of the components of the electric field gradient tensor. To take account of crystal symmetry, we choose a different coordinate system from that used previously. Let xyz be a principal coordinate system fixed with respect to the crystal so that $\bar{V}_{xy} = \bar{V}_{yz} = \bar{V}_{xz} = 0$. The x , y and z axes are traditionally chosen so that

$$|\bar{V}_{zz}| \geq |\bar{V}_{yy}| \geq |\bar{V}_{xx}|. \quad (2.37)$$

It is also convenient to define two parameters q and η by

$$eq = \bar{V}_{zz} \quad (2.38)$$

$$\eta = (\bar{V}_{xx} - \bar{V}_{yy}) / \bar{V}_{zz}. \quad (2.39)$$

The electric field gradient tensor components obey Laplace's equation $\nabla^2 V = 0$. Thus, η satisfies the condition

$$0 \leq \eta \leq 1. \quad (2.40)$$

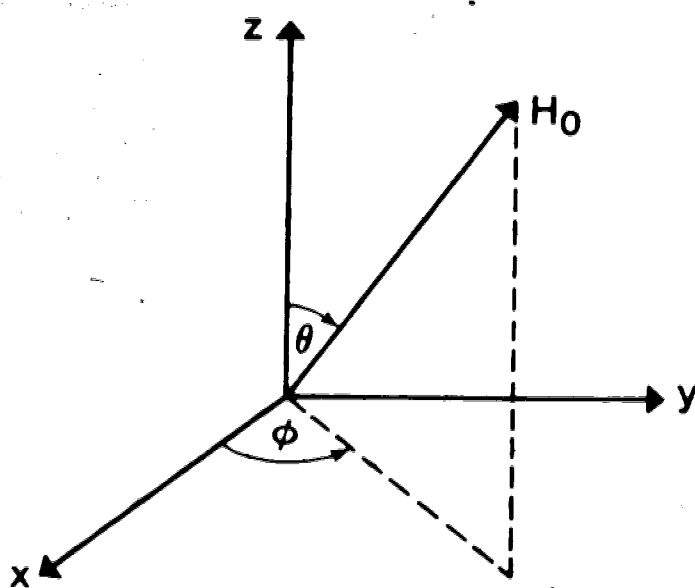
If the nuclei are situated on 3-fold, 4-fold or 6-fold axes of symmetry, \bar{V}_{xx} and \bar{V}_{yy} are equal and η is zero. Therefore η is called the "asymmetry parameter".

We denote the polar and azimuthal angles of the external magnetic field \vec{H}_0 with respect to the crystal coordinate system (xyz) by θ and ϕ respectively, as shown in Fig. 2.3. By transforming Eq. (2.36) from the laboratory coordinate system to the crystal coordinate system, it can be shown that

$$\begin{aligned} E_m = & -\gamma \hbar m H_0 + \frac{3Aeq}{2} (3\cos^2\theta - 1 + \eta \sin^2\theta \cos 2\phi) \left\{ m^2 - \frac{1}{3} I(I+1) \right\} \\ & + \frac{A^2 e^2 q^2}{4h\nu_0} \left[2m \{ 4I(I+1) - 1 - 8m^2 \} \left\{ \frac{9}{4} \sin^2 2\theta - \frac{3}{2} \eta \sin^2 2\theta \cos 2\phi \right. \right. \\ & + \left. \left. \eta^2 (\sin^2\theta - \sin^4\theta \cos 2\phi) \right\} - \frac{m}{2} \{ 2I(I+1) - 1 - 2m^2 \} \{ 9\sin^4\theta \right. \\ & \left. + 6\eta \sin^2\theta \cos 2\phi (2 - \sin^2\theta) + \eta^2 (\cos^2 2\phi \sin^4\theta + 4(1 - \sin^2\theta)) \right], \end{aligned} \quad (2.41)$$

Figure 2.3

Orientation of the external magnetic field relative to the principal axes of the crystal.



where ν_0 is the unperturbed frequency $\gamma H_0/2\pi$.

The frequencies of the quadrupole split NMR lines are given by

$$|E_{m-1} - E_m|/\hbar. \quad (2.42)$$

For a spin system with $I = 3/2$, it can be shown by using Eqs. (2.41) and (2.42) that the frequency of the so-called centre line, corresponding to the transition $m = 1/2 \leftrightarrow -1/2$, is given by

$$\nu_c = \nu_0 - \frac{e^2 q Q^2}{192 h^2 \nu_0} [9 \sin^2 \theta (9 \cos^2 \theta - 1) - 6 \eta \sin^2 \theta \cos 2\phi] \left\{ \right. \\ \left. (10 - 9 \sin^2 \theta) - 4 \eta^2 (1 - 3 \sin^2 \theta + \frac{9}{4} \sin^4 \theta \cos 2\phi) \right\}. \quad (2.43)$$

Also the frequencies ν_{\pm} of the so-called satellites, corresponding to the transitions $m = 3/2 \leftrightarrow 1/2$ and $m = -1/2 \leftrightarrow -3/2$, are given by (for + positive γ).

$$\nu_{\pm} = \nu_0 \mp \frac{e^2 q Q}{4 h} (3 \cos^2 \theta - 1 + \eta \sin^2 \theta \cos 2\phi) + \frac{e^4 q^2 Q^2}{24 h^2 \nu_0} \left\{ \frac{9}{4} \sin^2 2\theta \right. \\ \left. - \frac{3}{2} \eta (\sin^2 2\theta \cos 2\phi) + \eta^2 \sin^2 \theta (1 - \sin^2 \theta \cos^2 2\phi) \right\}. \quad (2.44)$$

We see from Eqs. (2.43) and (2.44) that, to first order, the centre line frequency is not perturbed by the quadrupole interaction, and the satellites are equally spaced relative to the centre line. In this approximation,

it follows that the centre line and both satellites overlap when

$$-3\cos^2\theta - 1 + \eta\sin^2\theta\cos 2\phi = 0 \quad (2.45)$$

However, it can also be shown from Eqs. (2.43) and (2.44) that, when account is taken of the second order terms, perfect resonance overlap will never occur. Thus, whether an approximate overlap of the centre line and satellites can be achieved, depends upon the relative magnitude of the second order quadrupole shift and the width of the individual NMR lines.

2.3 Orientation dependence of the nuclear quadrupole spin-lattice relaxation in crystals.

Examination of Eqs. (2.31), (2.32) and (2.33) in the previous section shows that the nuclear quadrupole Hamiltonian couples Zeeman states whose m values differ by ± 1 and ± 2 . Using Fermi's Golden Rule, the probability of transitions where m changes by ± 1 and ± 2 is given by

$$W_{m \rightarrow m+1} = \frac{2\pi\lambda_1^2}{\hbar} \frac{\sum_{nn'} \exp(-\beta E_n) |\langle n' | V_{x',z'} - iV_{y',z'} | n \rangle|^2 \delta(E_{n'} - E_n + E_{m+1} - E_m)}{\sum_n \exp(-\beta E_n)} \quad (2.46)$$

and

$$W_{m \rightarrow m+2} = \frac{2\pi\lambda_2^2}{\hbar} \frac{\sum_{nn'} \exp(-\beta E_n) |\langle n' | \frac{1}{2}(V_{x',x'} - V_{y',y'}) - iV_{x',y'} | n \rangle|^2 \delta(E_{n'} - E_n + E_{m+2} - E_m)}{\sum_n \exp(-\beta E_n)} \quad (2.47)$$

where

$$\lambda_1 = A(2m+1)[(I-m)(I+m+1)]^{\frac{1}{2}}$$

$$\lambda_2 = A[(I-m)(I-m-1)(I+m+1)(I+m+2)]^{\frac{1}{2}}$$

In Eqs. (2.46) and (2.47), the electric field gradient operators such as $V_{x'z'}$, are viewed from the laboratory coordinate system $x'y'z'$ in which the external magnetic field lies along the z' direction. Also β is $1/kT_L$, T_L is the lattice temperature, and n and n' are the initial and final lattice states respectively. It is convenient to define (cf. Yosida and Moriya, 1956) two quantities W_1 and W_2 , which characterize the nuclear quadrupole spin-lattice relaxation. They are defined by the expressions

$$W_{m \rightarrow m+1} = \frac{W_1 (2m+1)^2 (I+m+1)(I-m)}{2I(2I-1)^2} \quad (2.48)$$

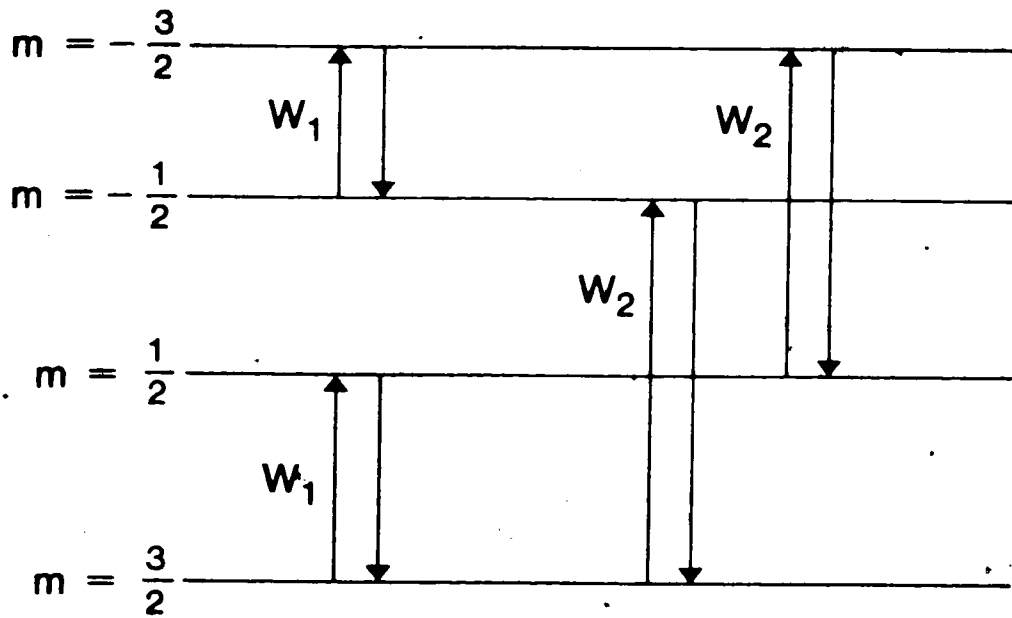
and

$$W_{m \rightarrow m+2} = \frac{W_2 (I-m)(I-m-1)(I+m+1)(I+m+2)}{2I(2I-1)^2} \quad (2.49)$$

For the case $I = 3/2$, with which we are concerned in this thesis, $W_{m \rightarrow m+1}$ is zero except when m equals $-3/2$ or $1/2$. Similarly, $W_{m \rightarrow m+2}$ is zero except when m equals $-3/2$ or $-1/2$. The electric quadrupole transitions for $I = 3/2$ are shown in Fig. 2.4. It follows from Eqs. (2.48) and (2.49) that

$$W_1 = \frac{\pi e^2 Q^2}{4I\hbar} \times \frac{\sum_{nn'} \exp(-\beta E_n) |\langle n' | V_{x'z'} - iV_{y'z'} | n \rangle|^2 \delta(E_{n'} - E_n + E_{m+1} - E_m)}{\sum_n \exp(-\beta E_n)} \quad (2.50)$$

Figure 2.4
Nuclear electric quadrupole transitions for $I = 3/2$.



and

$$W_2 = \frac{\pi e^2 Q^2}{4I\hbar} \times \frac{\sum_{nn'} \exp(-\beta E_n) |\langle n' | \frac{1}{2}(V_{x'x} - V_{y'y}) - iV_{x'y} | n \rangle|^2 \delta(E_n, -E_n + E_{m+2} - E_m)}{\sum_n \exp(-\beta E_n)} \quad (2.51)$$

It is clear from Eqs. (2.50) and (2.51) that W_1 and W_2 depend upon the direction of z' , and hence the direction of the external magnetic field, relative to the crystal. It can be shown (Hughes, 1973) by means of the principle of time reversal invariance that the general orientation dependence of W_1 and W_2 is of the form

$$\begin{aligned} W \sim & c_1^{(\mu)} + c_2^{(\mu)} \sin 2\theta + c_3^{(\mu)} \sin^4 \theta + \sin \theta \cos \theta (c_4^{(\mu)} \cos \phi + c_5^{(\mu)} \sin \phi) \\ & + \sin^3 \theta \cos \theta (c_6^{(\mu)} \cos \phi + c_7^{(\mu)} \sin \phi) + \sin^2 \theta (c_8^{(\mu)} \cos 2\phi \\ & + c_9^{(\mu)} \sin 2\phi) + \sin^4 \theta (c_{10}^{(\mu)} \cos 2\phi + c_{11}^{(\mu)} \sin 2\phi) \\ & + \sin^3 \theta \cos \theta (c_{12}^{(\mu)} \cos 3\phi + c_{13}^{(\mu)} \sin 3\phi) \\ & + \sin^4 \theta (c_{14}^{(\mu)} \cos 4\phi + c_{15}^{(\mu)} \sin 4\phi), \end{aligned} \quad (2.52)$$

where θ and ϕ are the polar and azimuthal angles of the external magnetic field measured relative to a crystal

coordinate system. The coefficients $c_i^{(\mu)}$ are in general linear combinations of the components of a real symmetric fourth-rank tensor (Pietila, 1968; Snyder and Hughes, 1971; Hughes, 1973)

$$M_{\alpha\beta\alpha'\beta'}(\mu, m) = \frac{2\pi}{\hbar} \frac{\sum_{nn'} \exp(-\beta E_n) \langle n' | V_{\alpha\beta} | n \rangle \langle n' | V_{\alpha'\beta'} | n \rangle \delta(E_n - E_{n'} + E_{m+\mu} - E_m)}{\sum_n \exp(-\beta E_n)} \quad (2.53)$$

where $\alpha, \beta, \alpha', \beta' = x, y, z$. Here xyz are the axes of a coordinate system fixed with respect to the crystal and chosen in such a way as to make full use of crystal symmetry. The tensor components $M_{\alpha\beta\alpha'\beta'}(\mu, m)$ are properties of the crystal. In general there are fifteen independent M-tensor components. However, the presence of crystal symmetry reduces this number. For example, for $\bar{3}$ and $2m$ symmetry there are four and six independent M tensor components respectively.

The approach to equilibrium of a spin system (with $I \geq 1$) is usually non-exponential. In general, the relaxation behaviour of a system of nuclei with spin number I is governed by $2I$ relaxation times (Andrew and Tunstall, 1961). For example, for $I = 3/2$, the approach to equilibrium is of the form

$$Ae^{-2W_1 t} + Be^{-2W_2 t} + Ce^{-2(W_1 + W_2)t}$$

where A, B and C are determined by the initial conditions. However, if a Boltzmann distribution can be established among the Zeeman levels of the spin system, the relaxation behaviour is exponential and the nuclear quadrupole spin-lattice relaxation time T_1 is given by (Andrew and Tunstall, 1961)

$$T_1^{-1} = [(2I+3)/5I(2I-1)](W_1+4W_2). \quad (2.54)$$

Spin exchanges (Andrew and Tunstall, 1961) maintain a Boltzmann distribution among the energy levels of a spin system if the various quadrupole-split resonances can be made to overlap. As pointed out in section 2.2, this can be achieved for a system of identical nuclei in a non-cubic crystal by suitably orienting the crystal relative to the external magnetic field, provided second order effects are sufficiently small.

For the case of relaxation mechanisms such as the two-phonon Raman process (Van Kranendonk, 1954; Van Kranendonk and Walker, 1967, 1968), the energy difference $E_{m-\mu} - E_m$ is negligible in comparison with typical lattice energies E_n in the delta function in Eqs. (2.50), (2.51) and (2.53). The M-tensor components associated with W_1 are therefore essentially equal to those associated with W_2 . By substituting in Eq. (2.50), it is then found (Hughes and Spencer, 1979) that

$$T_1^{-1} = \frac{e^2 Q^2 (2I+3)}{80I^2 (2I-1)} [k_1 + k_2 \sin^2 \theta + \sin \theta \cos \theta (k_3 \cos \phi + k_4 \sin \phi) + \sin^2 \theta (k_5 \cos 2\phi + k_6 \sin 2\phi)], \quad (2.55)$$

where the coefficients k_i are linear combinations of the M-tensor components. The angles θ and ϕ are not independent, since they must satisfy Eq. (2.45) for resonance overlap. By eliminating θ using Eq. (2.45) it can be shown that

$$T_1^{-1} = \frac{e^2 Q^2 (2I+3)}{80I^2 (2I-1)} \left\{ k_1 + \frac{2k_2 + [2(1-n\cos 2\phi)]^{1/2} (k_3 \cos \phi + k_4 \sin \phi)}{3 - n\cos 2\phi} + \frac{2(k_5 \cos 2\phi + k_6 \sin 2\phi)}{3 - n\cos 2\phi} \right\}. \quad (2.56)$$

Because of crystal symmetry, some of the coefficients vanish. Thus, for ^{23}Na in single crystals of NaNO_3 where the point group symmetry is $\bar{3}$, it can be shown by using Eq. (2.56) that

$$T_1^{-1} = (e^2 Q^2 / 60) (8 M_{1111} + 8 M_{3131} + M_{3333}). \quad (2.57)$$

We note that T_1 is independent of the orientation of the crystal relative to the external magnetic field. This is not the case in general. For example for ^{23}Na in NaNO_2 where the point group symmetry is $mm2$, T_1 is given by

$$\begin{aligned}
T_1^{-1} = \frac{e^2 Q^2}{30} & (4M_{1111} + 4M_{1212} + 4M_{1133} + M_{3131} + M_{2323} + M_{3333} \\
& + \frac{3}{3-n\cos 2\phi} [M_{3131} + M_{2323} + M_{3333} - 2M_{1111} - 2M_{1212} \\
& - 2M_{1133} + (M_{3333} + 2M_{1133} + M_{2323} - M_{3131}) \cos 2\phi] \} :
\end{aligned}
\tag{2.58}$$

(

CHAPTER 3
EXPERIMENTAL DETAILS AND RESULTS

3.1 Apparatus

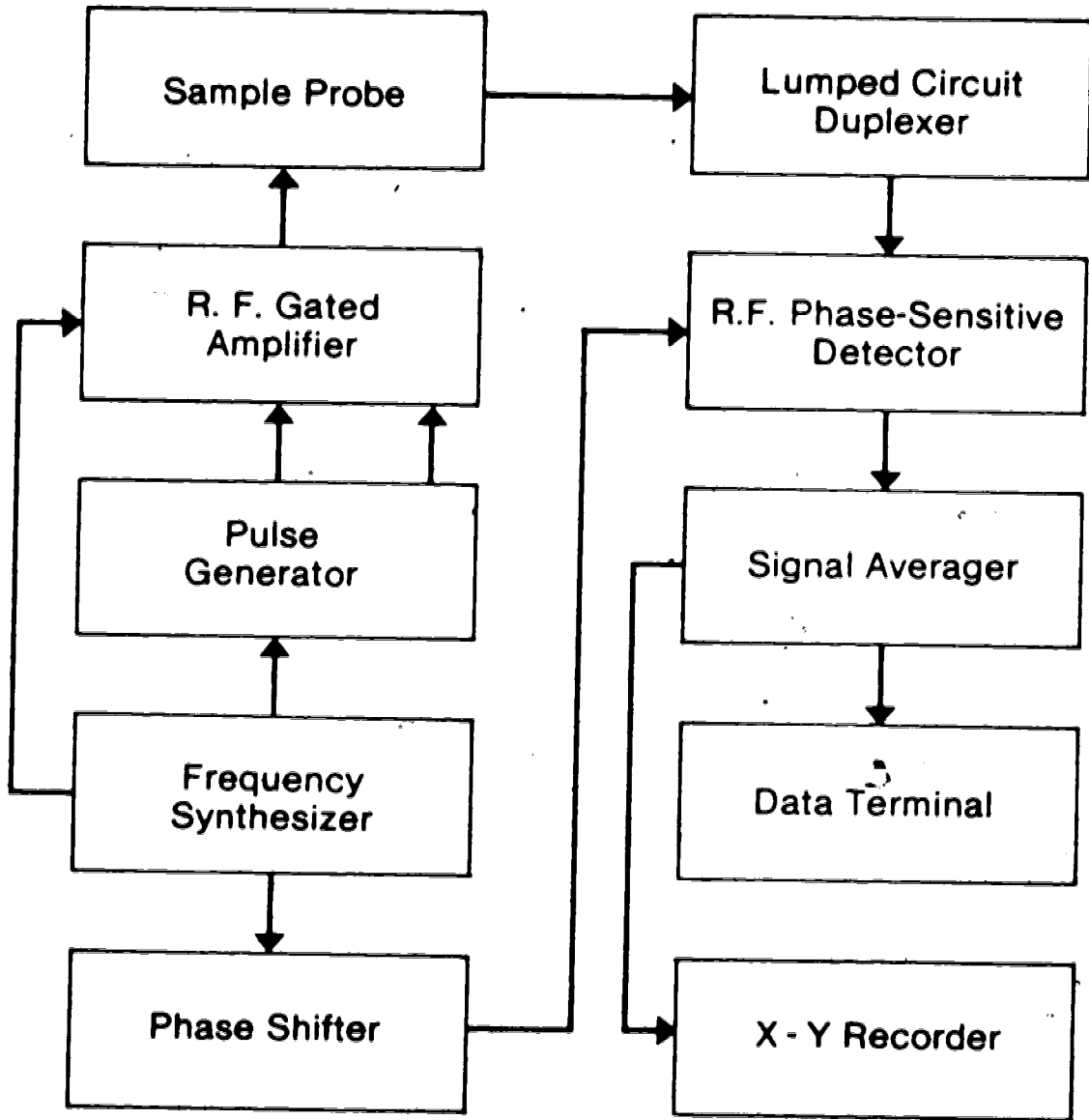
3.1.1 Brief description of the pulsed NMR spectrometer

In this section we briefly describe the various parts of the apparatus and their functional relationships. Important parts of the apparatus are described in more detail in sections 3.1.2 to 3.1.7.

A block diagram of the apparatus is shown in Fig. 3.1. A Takeda-Riken 3130 frequency synthesizer supplies a cw signal to a Matec 515 rf gated amplifier. The gating signal is provided by a pulse generator. The second connection between the pulse generator and the rf gated amplifier carries the reset pulses to be discussed later. The clock pulses for the pulse generator are derived from a cw signal fed from the frequency synthesizer. This ensures that the gating pulses produced by the pulse generator are coherent with the rf signal being gated. The frequency synthesizer also provides a cw reference signal to the phase-sensitive detector. This signal is passed through a phase shifter in order to allow adjustment of the phase of the reference signal. The phase shifter uses a variable 10-turn delay line to provide the phase variation.

The output from the rf gated amplifier feeds a

Figure 3.1
Block diagram of the system.



single NMR coil in which the sample is located. A lumped circuit duplexer is used to decouple the NMR coil and the rf phase-sensitive detector when the rf pulses are on. When rf pulses are off, the NMR coil is coupled to the rf phase-sensitive detector so that the (weak) NMR signals can be amplified and detected. The phase-detected NMR signal is fed to a Nicolet 1170 signal averager.* The averaged NMR signal can be viewed on a CRT, digitally read out via a Texas Instruments type 733 ASR electronic data terminal or read out on a Hewlett-Packard 7035B X-Y recorder.

3.1.2 Sample probe

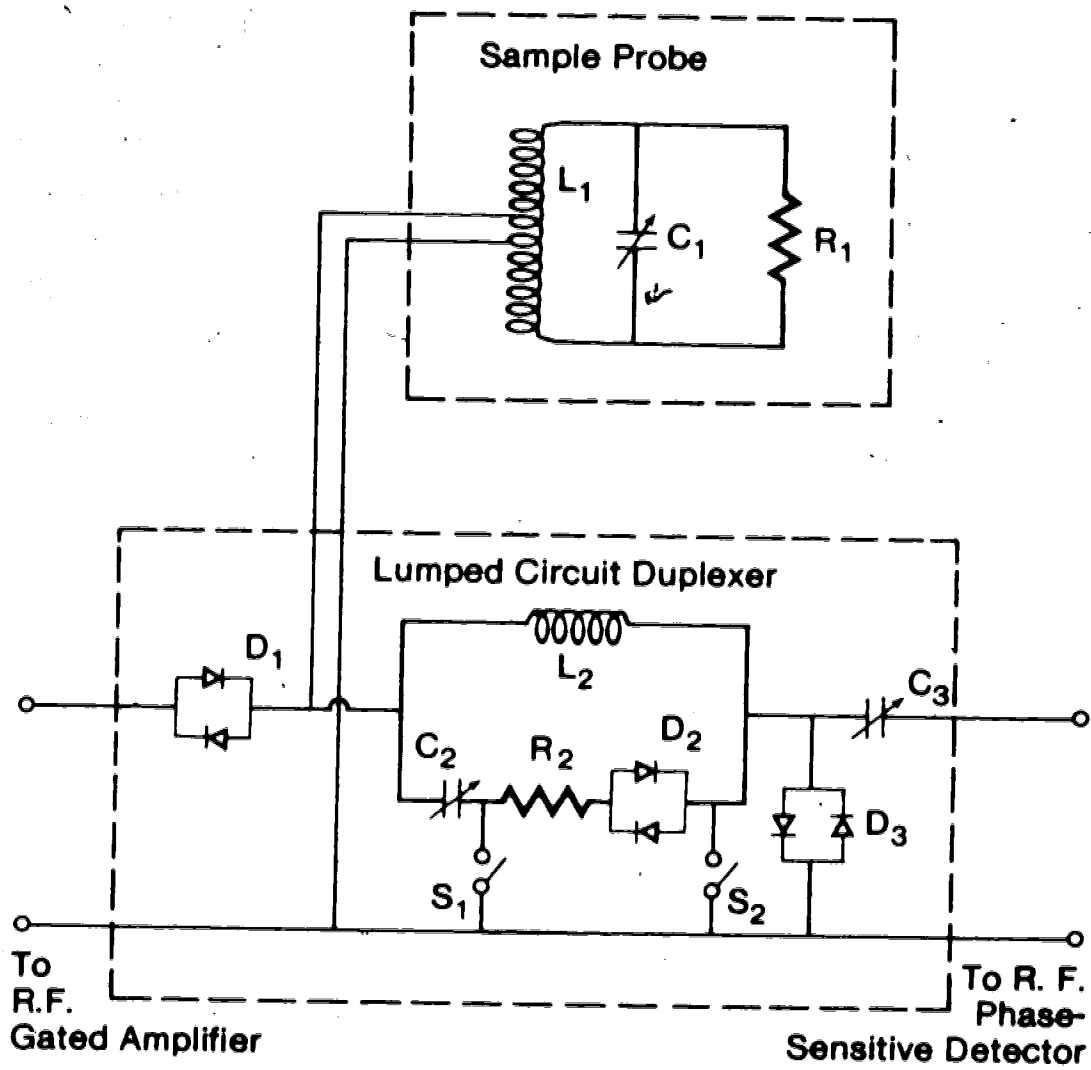
The NMR sample coil has a length of 0.8 inches and a diameter of 0.58 inches. It consists of 21 turns of silver wire 0.0125 inches in diameter and has a measured inductance of approximately $7\mu\text{H}$. Silver was chosen in preference to copper because the NMR frequency of copper is close to that of sodium, and it was important to ensure that no background NMR signals were present.

The NMR coil, represented by the inductance L_1 in Fig. 3.2, is connected to a variable 5-50 pF capacitor C_1 . In order to avoid dielectric breakdown caused by the high voltages present during the rf pulses, a vacuum capacitor from ITT Jennings Ltd. was used for C_1 .

*I am grateful to the Department of Physics, University of Calgary, in particular Dr. A.W. Harrison, for the loan of the Nicolet 1170 signal averager.

Figure 3.2

Circuit diagram of the sample probe and the lumped circuit duplexer.



The capacitor was physically small enough to be located adjacent to the NMR coil within the sample probe. This kept stray capacitance to a minimum and allowed the NMR coil to have as many as twenty-one turns. A ferromagnetic bearing on the capacitor was replaced by a nylon one so as not to disturb the homogeneity of the external magnetic field.

The output impedance of the rf gated amplifier is 50Ω whereas the impedance of the L_1C_1 combination at resonance is several tens of thousands of ohms. An impedance match was obtained by connecting the rf gated amplifier across a single turn of the NMR coil as shown in Fig. 3.2. Connection across the single turn was achieved by soldering two lengths of silver wire 0.0125 inches in diameter to the coil. The tapped-coil behaves like a transformer, and the impedance ratio is thus approximately the square of the turns ratio, i.e. 21^2 or 441. The input impedance of the NMR coil (measured across the single turn) was found to be about 100Ω at an operating frequency of 14.5 MHz when C_1 was tuned to resonance. A resistor was therefore connected across L_1 and C_1 and the value was chosen so that the input impedance was 50Ω and resistive at the operating frequency. The impedance measurements were made using a Hewlett Packard 4815A rf vector impedance meter.* Since the output impedance of the rf gated

*I am grateful to the Department of Electrical Engineering, University of Alberta, for the use of the Hewlett Packard 4815A rf vector impedance meter.

amplifier is also 50Ω , the sample probe and gated amplifier are connected by ordinary 50Ω (RG-58) coaxial cable. This impedance match ensures maximum power transfer from the amplifier to the probe.

To our knowledge, this is the first time such a tapped coil arrangement has been used. Most other NMR spectrometers use a matching network consisting of several components. The tapped coil arrangement is simple and is also capable of generating large rf magnetic fields with a relative modest power amplifier.

It is important that the Q factor of the NMR coil should not be too high. Otherwise, fast rise and fall times for the rf pulses cannot be obtained. The Q factor of the sample tuned circuit was found to be 34, and this is low enough for work on ^{23}Na nuclei.

The probe body was solidly constructed to reduce microphonic effects. Brass was used in the construction, in preference to aluminum for example, to reduce spurious ringing signals observed by other workers (Buess and Petersen, 1978) and also observed by ourselves with a preliminary aluminum probe.

3.1.3 Lumped circuit duplexer

In our apparatus, a single coil is used instead of a crossed coil configuration. Thus, it is necessary to isolate the detector from the output of the rf gated amplifier. One method is to connect the NMR coil to the

rf phase-sensitive detector by means of a quarter wavelength transmission line, with crossed diodes connected across the input to the detector. During a pulse, the diodes are turned on and therefore present a low impedance. The quarter-wavelength transmission line is thus shorted so that its input impedance becomes infinite. In the absence of a pulse, the diodes present a high impedance so that the transmission line is open-circuited. It therefore presents a low impedance and thus allows the NMR signal to pass to the rf phase-sensitive detector.

The circuit described by McLachlan (1980) shown in Fig. 3.2 replaces the quarter-wavelength transmission line by lumped circuit components, and has superior performance to a transmission line. When a rf pulse is applied, the crossed diode pairs D_1 , D_2 and D_3 conduct and L_2 , C_2 and R_2 form a parallel tuned resonant circuit which presents a high impedance at the resonance frequency. The voltage appearing across D_3 which are fast silicon diodes is about 0.6 V RMS. The capacitor C_3 , in conjunction with the 50 Ω input impedance of the rf phase-sensitive detector, attenuates the voltage further so that only about 0.06 V RMS reaches the detector. When there is no rf pulse, all the diodes are open-circuited, and L_2 and C_3 form a series tuned resonant circuit. This presents a low impedance at resonance and allows the NMR signal to pass to the rf phase-sensitive detector.

The purpose of the crossed diodes D_1 is to connect

the rf gated amplifier to the NMR coil during the pulses, and to isolate it when the rf pulses are absent. The series resonant circuit is tuned by feeding a signal at the operating frequency into the probe terminal. The amplitude should be small enough so as not to turn on the crossed diodes. The capacitor C_3 is tuned for maximum rf signal entering the rf phase-sensitive detector. To tune the parallel resonant circuit, switches S_1 and S_2 are closed, and C_2 is varied to obtain maximum input impedance at the probe terminal.

3.1.4 R.F. phase-sensitive detector

NMR signals are detected by a Matec 615 tuned rf phase-sensitive detector. A cw level control adjusts the amplitude of the reference signal entering the rf phase-sensitive detector. For the work described in this thesis, the control was set at maximum at which setting the cw reference level indicator read 17%. The unit is provided with high impedance and low impedance inputs. The low (50Ω) impedance input was used in order to match the impedance of the tapped NMR coil. The unit is also equipped with high-Q and low-Q rf amplifier stages. The high-Q amplifier stage was used in our work because of the better signal to noise ratio it provides. (The low-Q amplifier has a shorter recovery time than the high-Q amplifier. However, we were more interested in a good signal to noise ratio than in a short recovery time.) The unit is equipped

with a control which enables the bandwidth to be varied between 0.9 kHz and 2500 kHz. For the work on a liquid sample, the bandwidth setting was B70, corresponding to a bandwidth of roughly 20 kHz. For the work on the crystals, the bandwidth setting was C70, corresponding to a bandwidth of roughly 200 kHz.

3.1.5 R.F. gated amplifier

The Matec 515 rf gated amplifier, when plugged into the Matec 5100 gating modulator, provides gated rf pulses with a maximum power of approximately 1 kW. The output impedance is 50 Ω . The pulses from the pulse generator are introduced through the "External Modulation" input. The amplifier is tuned by adjusting the "R.F. Tuning" control for maximum output when a 50 ohm resistor is connected to the amplifier output.

3.1.6 Signal averager

The signal averager system consists of a Nicolet 1170 high-speed signal averager with a Nicolet 171/2 signal digitizer plug-in unit. The data acquisition time can be varied from 1 μ s to 99.9 s per point. A post-trigger delay ranging from 1 μ s to 99.9 s can be introduced. Total memory consists of 2048 channels. The capacity of each channel is 20 bits.

The signal digitizer plug-in receives analog signals, digitizes them and transfers the information to the high-


speed signal averager. The analog-to-converter resolution is 6, 9, or 12 bits. The 12 bit resolution was used in the present work. For preliminary work on a liquid sample, a Fabritek 1062 signal averager was used. However, the slow acquisition rate of 200 μ s per point made it unsuitable for work on the solid samples.

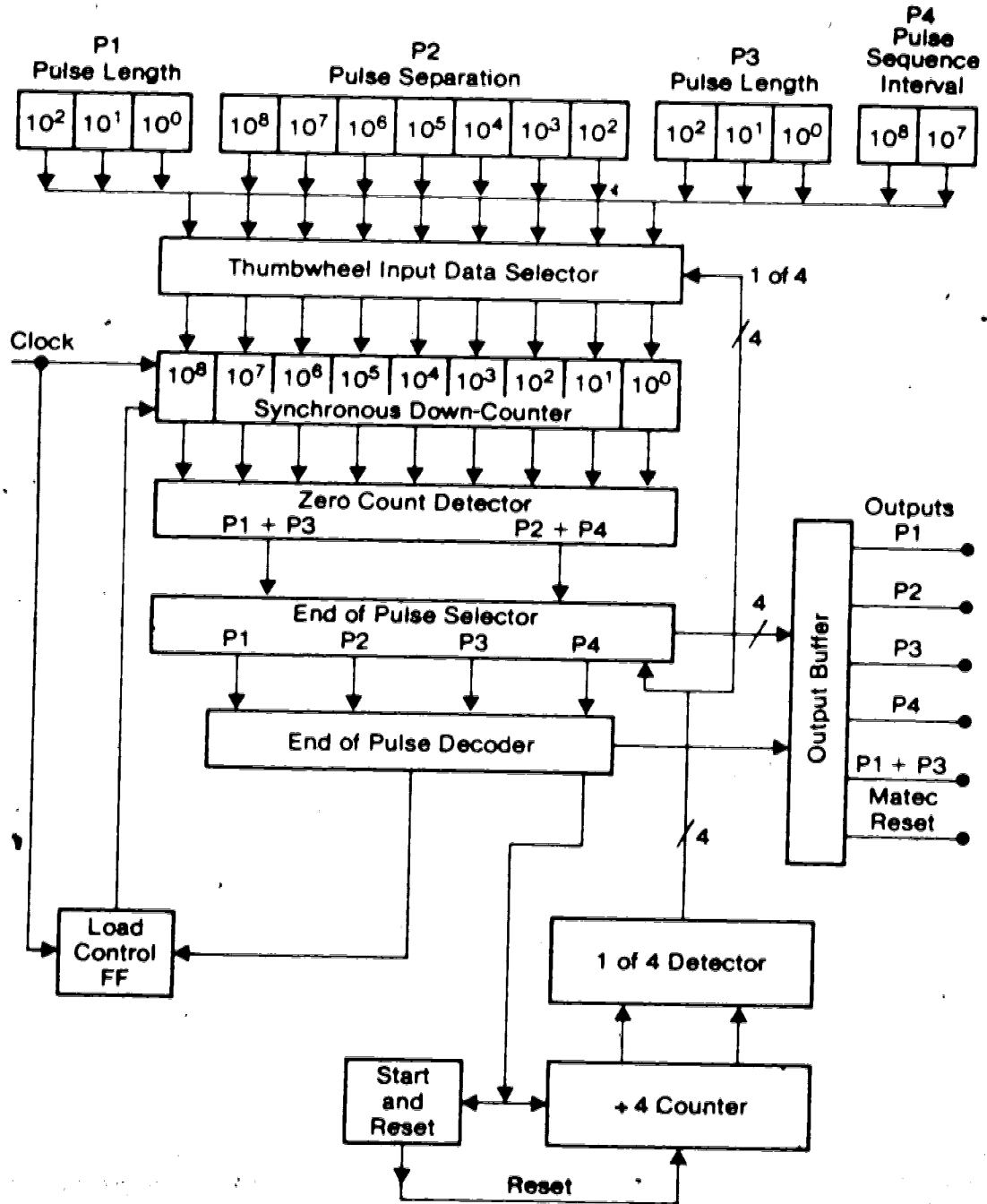
3.1.7 Pulse generator

The pulse generator used in our system was designed and constructed by the electronic shop in the Department of Physics. A schematic diagram is shown in Fig. 3.3. A synchronous down-counter is driven by a clock signal which is obtained from the frequency synthesizer. The initial settings of the down-counter are determined by one of four sets of decade thumbwheel switches, P1, P2, P3 and P4. The first set consists of three decade switches which can be set between 0 and 999. These determine the length of the first pulse between 1 and 1000 clock periods. (The extra clock period is caused by a time delay in the circuitry.) The second set consists of a set of decade switches which can be set between 10^2 and 9.999999×10^8 . These determine the separation time between the first and second pulse. The third set determines the length of the second pulse between 1 and 10^3 clock periods. The fourth set determines the pulse sequence interval, or the time between the second pulse and the first pulse if the pulse sequence is repeated. It can be set between 10^7

Figure 3.3

Schematic diagram of the pulse generator. The arrows indicate the direction of information flow.





and 9.9×10^8 clock periods. Since the operating frequency is 14.5 MHz, the pulse lengths can be varied up to 69 μ s, and the pulse separation and pulse sequence interval can be varied up to 69 seconds.

At the beginning of a cycle, data is loaded from P1 into the synchronous down-counter via the thumbwheel input data selector. When the counter reaches zero, data gate P1 is closed and data gated P2 is opened so that the data from the P2 thumbwheel switches are loaded into the counter. When the counter reaches zero, data gate P2 is closed and P3 is opened and the procedure continues until the counter has counted down to zero for P4. The logic signals are fed to the output buffer.

Individual outputs corresponding to P1, P2, P3 and P4 are provided. For experiments where single pulses are required, output P1 or P3 is used. In another output, P1 and P3 are added and this provides the gating signal for a two-pulse sequence such as the $180^\circ - \tau - 90^\circ$ sequence used in our experiments. The output buffer also provides narrow pulses which occur at the end of each of P1, P2, P3 and P4. These are used to reset a pair of flip-flops in the rf gated amplifier for the reason to be mentioned in section 3.3.

3.2 Details of Sample

3.2.1 Description of the sodium nitrate crystal

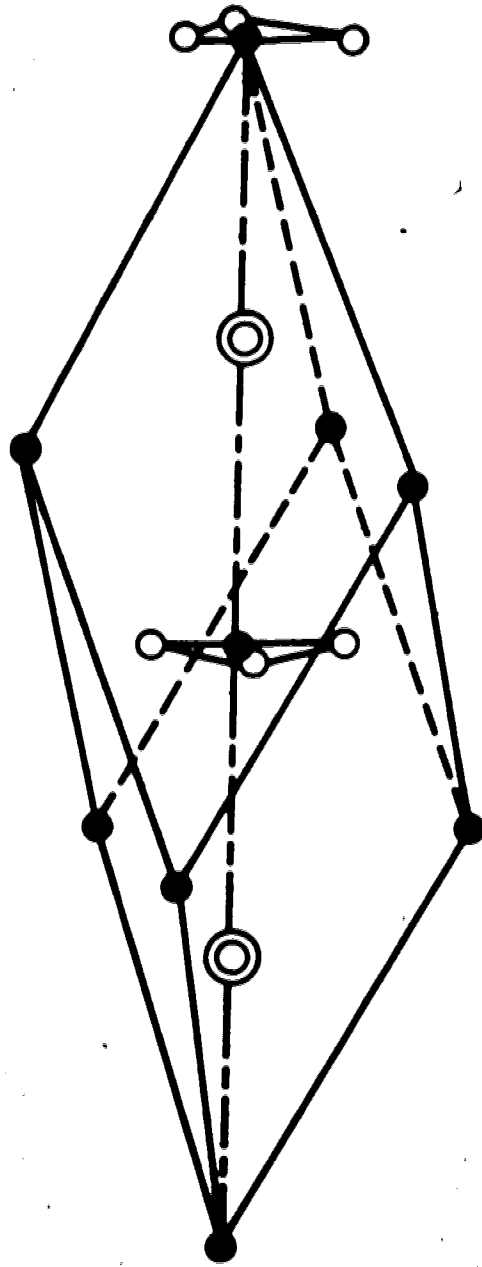
The sodium nitrate single crystal used in the work was the same one as used by Spencer and Hughes (1978). It was obtained from the Harshaw Chemical Company, Cleveland, U.S.A. and a spectroscopic analysis provided by Harshaw indicated the following impurities: Al, 3 ppm; Ca, 8 ppm; Mg, 3 ppm; Cu < 1 ppm; Si < 1 ppm. The crystal is in cylindrical form, 15 mm in diameter and 11 mm in length. The three-fold axis of symmetry is accurately parallel to the end faces of the cylinder.

3.2.2 Crystallography of NaNO₃

The unit cell of NaNO₃ is shown in Fig. 3.4. This material crystallizes in the rhombohedral system (space group $R\bar{3}c$, D^6_3d) with two molecules per unit cell. There are nitrogen atoms at each corner of the cell and at $1/2, 1/2, 1/2$; the sodium atoms are situated at $1/4, 1/4, 1/4$ and $3/4, 3/4, 3/4$ as shown in Fig. 3.4. The nitrate groups are planar, each nitrogen atom being situated at the centroid of an equilateral triangle of oxygen atoms whose plane is perpendicular to the three-fold axis. The sides of the oxygen triangles lie parallel to the projection of the cell edges on a plane perpendicular to the three-fold axis, the orientation of the triangles alternating by 180° along the three-fold axis. There are

7

Figure 3.4
Unit cell of sodium nitrate



⊙ Na

● N

○ O

•

two sodium atoms, situated at sites A and B say, per unit cell of NaNO_3 crystal. These sodium atoms have a similar environment possessing $\bar{3}$ symmetry. However, the environments are in each case differently oriented in space. These sodium nuclei have different intrinsic quadrupole relaxation probabilities, W_{1A} , W_{1B} , W_{2A} , and W_{2B} (Hughes and Reed, 1971). However, the time-averaged electric field gradient \bar{V}_{zz} ($= -2\bar{V}_{xx} = -2\bar{V}_{yy}$), which determines the quadrupole splitting (Cohen and Reif, 1957), has the same value at the A and B sites. The resonances from ^{23}Na nuclei at these sites therefore overlap. Since $I = 3/2$ for ^{23}Na , the NMR spectrum consists of three lines, the so-called centre line and satellites (see section 2.2). Even though the A and B nuclei in general have different intrinsic quadrupole relaxation probabilities, they are strongly coupled by spin exchanges (Abragam and Proctor, 1958; Bloembergen et al., 1959; Andrew and Swanson, 1960), which result from the overlapping of the resonances. Thus, the ^{23}Na nuclei in NaNO_3 behave as a system of identical nuclei, if crystal imperfections are ignored. The effective quadrupole relaxation probabilities W_1 and W_2 are the arithmetic means of W_{1A} and W_{1B} , and W_{2A} and W_{2B} respectively (Hughes and Reed, 1971).

3.3 Preliminary check of the equipment

In nuclear magnetic resonance, the higher the frequency, the better the signal to noise ratio. Also, in

our work it was necessary to achieve good overlapping of the component lines of the quadrupole split spectrum. To achieve this, the second order quadrupole splitting must be small and this, in turn, means that the NMR frequency must be high (see Eqs. (2.43) and (2.44)). However, the maximum usable frequency is determined by the magnetic field strength available. We worked with a field of approximately 13 kilogauss, which is close to the maximum field of our magnet. The gyromagnetic ratio of the ^{23}Na nucleus is such that the NMR frequency in a field of 13 kilogauss is 14.5 MHz. This is the frequency for which the sample probe was designed (see section 3.1.2).

The performance of the pulsed NMR spectrometer was checked using the ^{23}Na signal from a 2 ml sample of a doped saturated aqueous solution of sodium nitrate. The doping consisted of approximately M/10 concentration of paramagnetic $\text{Fe}(\text{NO}_3)_3$ in order to reduce the spin-lattice relaxation time to the order of 10 ms. This is done so that the spin system could recover quickly from the effects of a pulse. This allows pulsed experiments to be repeated at frequent intervals.

The gain of the rf gated amplifier was turned up to maximum, at which setting the voltage at the input to the NMR coil (across the single turn) was 600 volts peak-to-peak (V_{pp}). This corresponds to approximately 10 kV_{pp} across the whole NMR coil. All the measurements reported in this thesis were carried out using this maximum pulse

amplitude. The FID immediately following each pulse was observed on an oscilloscope connected to the video output of the rf phase-sensitive detector. The oscilloscope was triggered by the trailing edge of the pulse. The repetition rate of the pulses was 1.4 seconds leaving plenty of time for the spin system to relax back to equilibrium between pulses. The strength of the magnetic field was varied until a proper FID was observed; if the field is off-resonance, the nuclear precession frequency is different from the frequency of the reference signal fed to the rf phase-sensitive detector and the observed signal has the form of a damped oscillation.

After the proper FID was obtained, the reference phase was adjusted in order to obtain a maximum signal. The length of the rf pulses was then adjusted until the amplitude of the FID was a maximum, i.e. until the pulse was a 90° pulse. The pulse length indicated by the setting on the pulse generator was approximately 115 rf periods or 7.9 μ s. This pulse length is quite short, bearing in mind the rf power available. It shows the effectiveness of our tapped-coil impedance match.

Careful observation of the amplitude of the FID following a pulse of approximately 90° showed an inconsistency. At certain pulse lengths, every fourth pulse was found to be four rf periods shorter than the others. The problem was overcome by resetting a pair of flip-flops in the rf gated amplifier to coincide with the beginning of

the pulses from the pulse generator, as suggested by Mr. E. Cairns and Mr. W. Siewert. This required a small modification to the circuit of the rf gated amplifier, and the provision of narrow 'reset pulses' obtained from the pulse generator.

In order to obtain a 180° - τ - 90° pulse sequence for measuring spin-lattice relaxation times, the length of the first pulse generated by the pulse generator was increased from zero until the amplitude of the FID immediately following the pulse was zero. The absence of a FID means that there is no transverse magnetization and this implies that the pulse is a 180° pulse. The length of the second pulse generated by the pulse generator was increased from zero until the amplitude of the FID immediately following the pulse was a maximum, i.e. so that the second pulse is a 90° pulse. The length of the 180° pulse was found to be 205 rf periods or 14.2 μ s. This is slightly less than twice the length of the 90° pulse. This is presumably because of phase shifts which occur at the leading and trailing edges of each pulse.

The operation of the equipment was checked by measuring T_1 of the ^{23}Na nuclei in the doped saturated aqueous solution of NaNO_3 . These measurements were made using the Fabritek 1062 Signal Averager, operating at its fastest data acquisition rate of 200 μ s/point.

As described in section 2.1.2, the approach to equilibrium of the z-component of magnetization following

a 180° pulse will be of the form

$$\ln (M_0 - M_z) = A - (\tau/T_1). \quad (3.1)$$

Experimentally M_0 can be found by measuring the amplitude of the FID following a 90° pulse and M_z can be found by measuring the amplitude of the FID following a 90° pulse applied at a time τ after a 180° pulse. Since the difference between M_0 and M_z is required, it is not necessary to measure the baseline of the FID, provided the baseline is the same in both cases. Examination of the baseline showed it to be quite stable, so that it was only necessary to measure the difference between the magnitude of the FID's associated with M_0 and M_z . These values were measured in the fifth channel of the Fabritek Signal Averager, i.e. 5 times 200 μ s or 1 ms after the 90° pulse. To obtain good signal to noise ratio, signals were recorded 32 times in the signal averager. In order to minimize any error due to a change in gain of the system, values of M_0 were measured between each M_z measurement. Thus, the sequence was $M_0, M_z(\tau_1), M_0, M_z(\tau_2), \dots, M_z(\tau_n), M_0$. The arithmetic mean of the two M_0 values on either side of a M_z value was used in determining $\ln (M_0 - M_z)$ in Eq. (3.1). The data shown in Fig. 3.5 falls on a straight line, in agreement with Eq. (3.1). The value of T_1 found from a least squares fit of the data to a straight line is 20.4 ms. Repeating the measurements gave values

ranging from 20.0 ms to 20.8 ms, showing reasonably satisfactory reproducibility. J

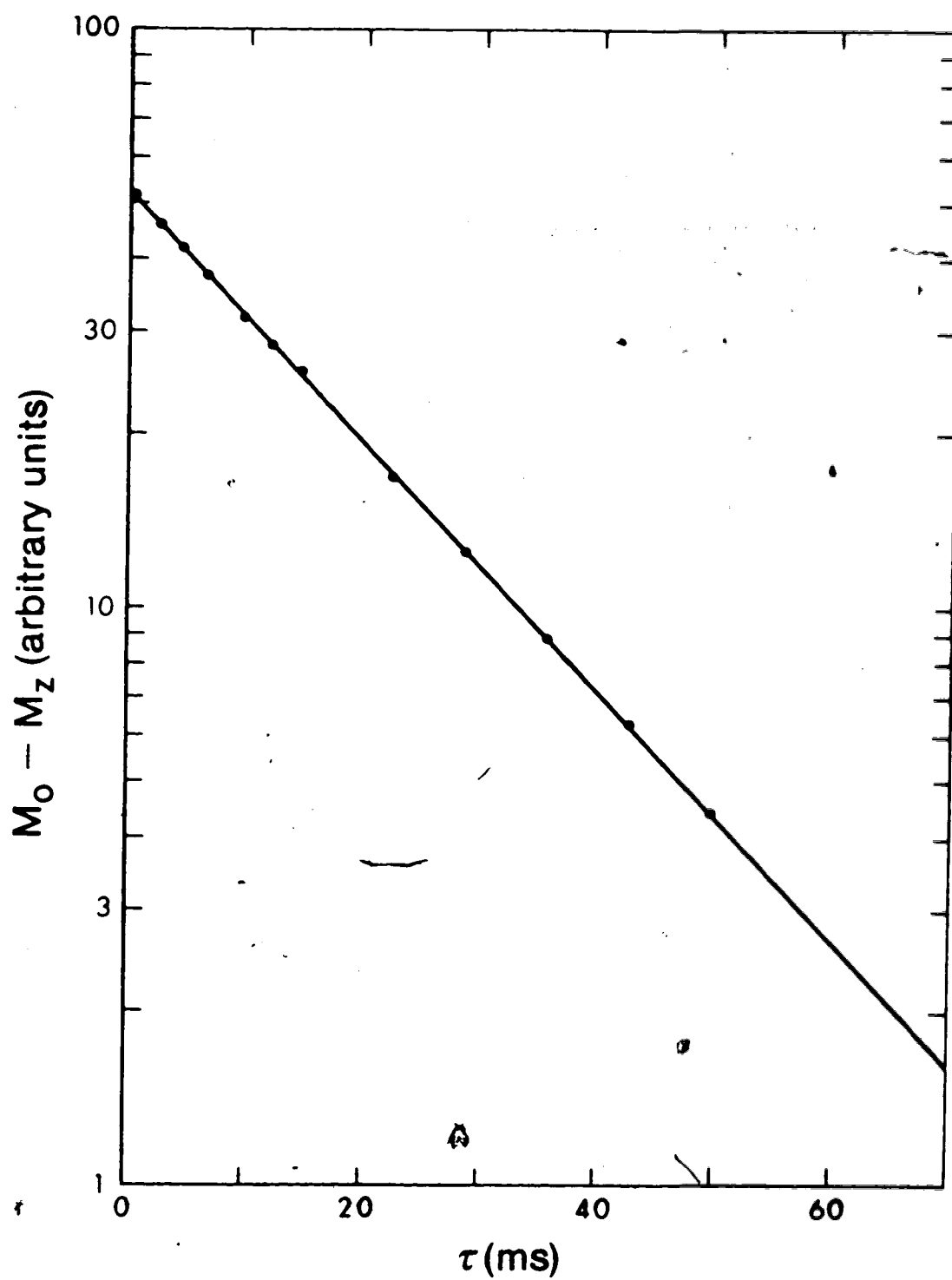
According to Andrew (1955), the spin-lattice relaxation time of protons in a M/10 aqueous solution of ferric ions is 1.15 ms. Since T_1 is inversely proportional to the square of the gyromagnetic ratio of the nucleus involved, and since the gyromagnetic ratio of the proton is 3.78 times as large as that of the ^{23}Na nucleus, the expected T_1 of ^{23}Na in a M/10 aqueous solution of ferric ions is 16.5 ms. Bearing in mind the uncertainty in the concentration and the simplifications made in the theory, the agreement between experiment and theory is satisfactory.

Examination of the M_0 values obtained with the doped aqueous solution of NaNO_3 showed no evidence of any systematic variation of M_0 with time. Thus, it was decided in future work to use the overall mean value of M_0 , rather than the mean of the M_0 values measured immediately before and after each M_z .

The data shown in Fig. 3.5 were taken with τ increasing monotonically throughout the experiment. This is not good practice, and it was decided in future to choose the τ values in a random order during the experiment. In this way, systematic errors due to a time-varying gain or baseline will show up as an enhanced scatter of the data points, rather than as a curvature of the data points in the semilogarithmic plot.

Figure 3.5

$M_O - M_Z$ versus pulse separation time τ for ^{23}Na in a doped saturated aqueous solution of NaNO_3 at 299K.



Examination of the data also showed the error in M_z was due to noise and was independent of the value of τ (and was also the same as the error in M_o). Thus, the error in the $M_o - M_z$ is the same for each data point. However, the error in $\ln(M_o - M_z)$ is inversely proportional to $(M_o - M_z)$ as can be seen by differentiation:

$$\delta \ln(M_o - M_z) = \delta(M_o - M_z) / (M_o - M_z). \quad (3.2)$$

Since $(M_o - M_z)$ varies by about an order of magnitude in a typical T_1 experiment, the random error associated with each data point also varies by about an order of magnitude. It is therefore important to perform a weighted least squares fit to the data. It is also helpful to determine the error in T_1 obtained from the least squares fit. The remaining T_1 values to be reported in this thesis were therefore obtained by means of a weighted least squares fit of the data. Also, two error estimates were obtained. One is derived from the scatter of the data about the straight line. The other is derived from the standard error associated with each data point. An estimate of this standard error can be obtained from the scatter in the various M_o values. The formulae required to perform a weighted least squares fit and to calculate the errors in the fitted parameters, are presented in Appendix 1. The method of obtaining the standard deviations and weighting factors needed in our least squares

fitting procedure are described in Appendix 2. A program for the Hewlett-Packard 67 programmable calculator that would calculate T_1 and the error in T_1 from values of $(M_0 - M_z)$ and τ is described in Appendix 3.

3.4 Measurement of the spin-lattice relaxation time of ^{23}Na in sodium chloride

In order to compare our T_1 values with those of other workers, and to look for possible systematic errors, we measured the spin-lattice relaxation time of ^{23}Na in a single crystal of NaCl at room temperature. Even though this T_1 is believed to be independent of crystal orientation relative to the external magnetic field (Zak, 1964; Snyder and Hughes, 1971), we aligned the crystal so that \vec{H}_0 was along the 100 direction.

Since the T_1 value is approximately 14 s (Schumacher, 1958; Satoh, 1965; Spencer and Hughes, 1978), the pulse sequence interval was set at its maximum value of 69 seconds or about $5T_1$, so that the starting magnetization is $(1 - 2e^{-5})M_0$ or $0.987 M_0$. Because of the long time between pulse sequences, the signals were averaged only 8 times, even though this sacrificed the signal to noise ratio.

According to the Matec manual, our rf phase-sensitive detector should be linear provided the video output is less than $1 V_{pp}$. We kept well below this limit by adjusting the receiver gain so that the maximum output was only $0.25 V_{pp}$. The bandwidth in the rf phase-sensitive detector was

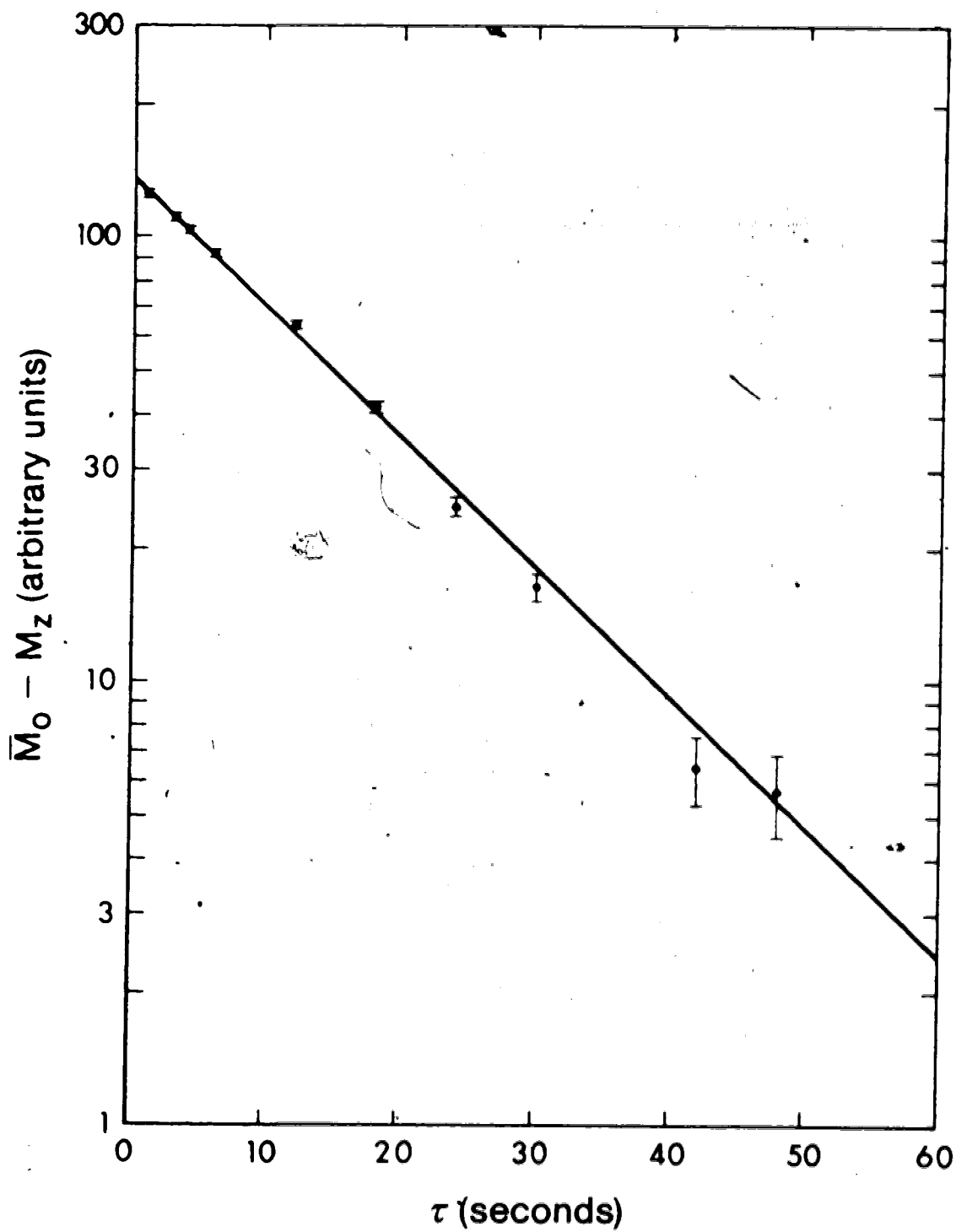
set at the position C70 corresponding to a bandwidth of roughly 200 kHz.

Since the decay of FID of ^{23}Na in NaCl at room temperature is much faster than the decay of the FID of ^{23}Na nuclei in the doped aqueous solution of NaNO_3 , a much faster data acquisition rate than the 200 μs per point of the Fabritek signal averager was needed. We therefore used the Nicolet 1170 signal averager, borrowed from the University of Calgary, for this work. A data acquisition rate of 1 μs per point was used. Also, a post trigger time delay of 28 μs was introduced so that the rf phase-sensitive detector output during the recovery period was not recorded. The τ values were selected in random order for the reason discussed in section 3.3. The FID signals were recorded in a quarter of the memory of the signal averager or 512 channels.

The data shown in Fig. 3.6 was obtained from the FID's recorded in the seventeenth channel of the signal averager. Thus, they were recorded $17+28 = 35 \mu\text{s}$ after the trailing edge of the 90° pulse. For an ideal crystal, the shape of the FID should be independent of τ . Thus, it should not matter where (i.e. at what time) the magnitude of the FID is measured, provided it is done consistently for all values of τ . (Traditionally, the magnitude of the FID has been measured as soon as possible after the 90° pulse). However, in order to check this point, we measured the FID's in the fourth, fifty-seventh

Figure 3.6

$\bar{M}_O - M_Z$ versus pulse separation time τ for ^{23}Na in NaCl
at 299K.



and ninety-seventh channels, in addition to the seventeenth channel. The values of T_1 were also obtained from the same FID's using data in the fourth, fifty-seventh and ninety-seventh channels. (These channels were far enough apart so that little correlation between the values is expected). The calculated T_1 values are shown in Table 1, together with the standard (68% confidence) error associated with the scatter and the standard error associated with the standard deviation per point. These two types of error estimates have been called external and internal errors respectively (Birge, 1932). It can be seen from the table that the two types of errors are of similar magnitude, indicating that the proper fitting function is a straight line. For purpose of calculation, the larger of the two errors was used in each case, as shown in the fifth column of Table 1. The weighted mean T_1 is 14.6 ± 0.15 seconds. This is compared with other published values in section 4.

Because the magnet enclosure was slightly warmer than room temperature, a thermometer was inserted into the sample probe (with rf pulses turned off) and the temperature was found to be 26°C . This was taken to be the sample temperature.

★

Table 1

T_1 of ^{23}Na in NaCl obtained using data from
different channels of the signal averager.

Channel number	T_1	Error (Scatter)	Error (Std. dev.)	T_1 (seconds)
4	14.37	0.20	0.22	14.37±0.22
17	14.91	0.30*	0.23	14.91±0.30
57	14.76	0.34	0.30	14.76±0.34
96	14.57	0.31	0.42	14.57±0.42

Weighted mean $T_1 = 14.60 \pm 0.15$ seconds.

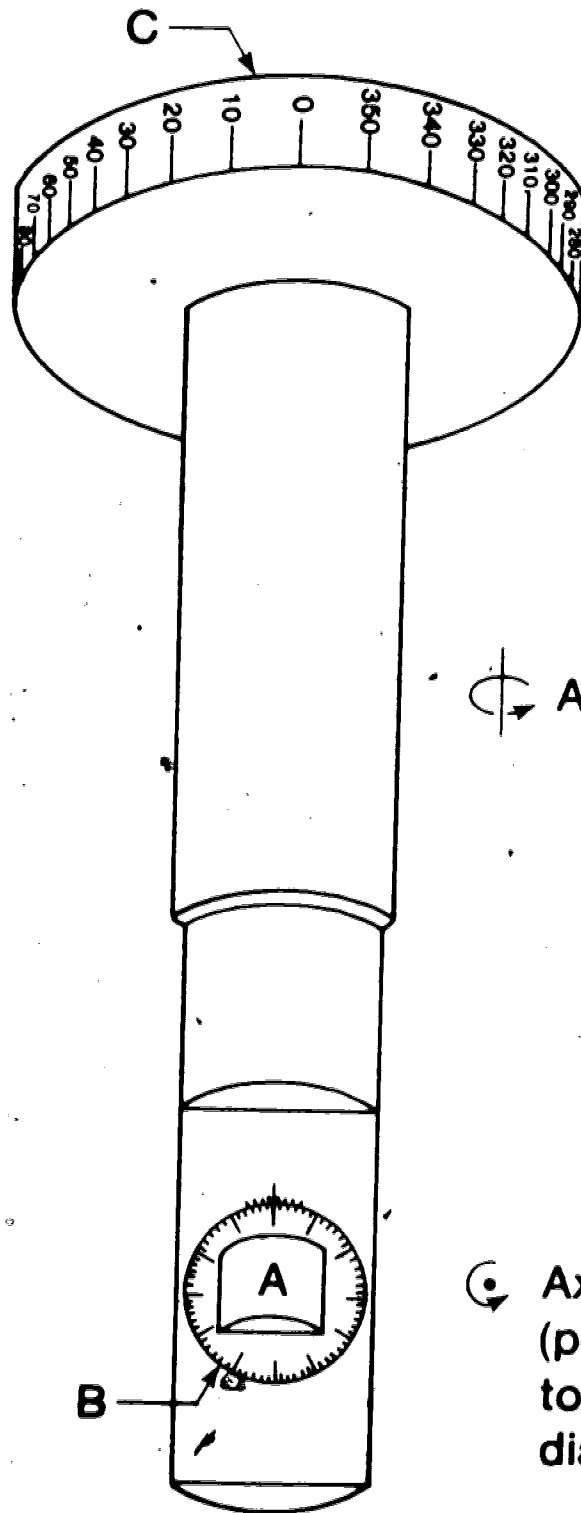
3.5 Measurement of the orientation dependence of the spin-lattice relaxation time of ^{23}Na in NaNO_3 .

3.5.1 Installation of the NaNO_3 crystal in the sample holder.

A special sample holder was constructed in such a way that it could be slid into the NMR coil and so that the crystal could be rotated independently about the two axes shown in Fig. 3.7. Axis 1 is the axis of the sample holder and the NMR coil. It is perpendicular to \vec{H}_0 . Axis 2 is perpendicular to axis 1. The crystal A was mounted in a collar B which can be rotated about axis 2. The collar is equipped with a vernier scale (see Fig. 3.7) so that its orientation can be read with an accuracy of about one degree. The sample holder can be rotated about axis 1 in the sample probe. The probe is equipped with a circular scale C and a vernier which can be read to within one tenth of a degree.

The crystal was aligned in the collar so that the three-fold axis was along axis 2. This was done in the following way. It can be shown from Eq. (2.44) that the separation of the two ^{23}Na satellite lines in NaNO_3 is a maximum at $\theta = 0$ (and 180°). The crystal was set in the collar so that the end faces are perpendicular to axis 1. This is the situation shown in Fig. 3.7. The sample holder was then rotated about axis 1 until the satellite separation was a maximum, i.e. until θ was 0° . This was

Figure 3.7
Diagram of the sample holder.



Axis 1

Axis 2
(perpendicular
to plane of
diagram)

achieved by setting the magnetic field to be on resonance for one of the satellites and rotating the crystal about axis 1 until the resonant magnetic field was a maximum or minimum, depending upon the satellite chosen. The crystal (and the collar) was then rotated through 90° about axis 2 and the sample holder was again rotated about axis 1 until the satellite separation was a maximum. This satellite separation was less than the value corresponding to $\theta = 0^\circ$ because axis 2 and the symmetry axis were not parallel to one another. The crystal was then rotated in the collar and the above measurements were carried out again. The process was repeated until there was no difference in the satellite separation when the crystal was rotated through 90° about axis 2. Axis 2 and the symmetry axis were then parallel to each other.

An important consequence of this adjustment is that rotation about axis 1 changes θ but not ϕ , whereas rotation about axis 2 changes ϕ but not θ . This situation greatly facilitates the measurements to be described in the remainder of this thesis.

3.5.2 Choice of crystal coordinate system for NaNO_3 .

In choosing the crystal coordinate system referred to in section 2.3 so as to make full use of crystal symmetry, the z axis is selected to coincide with the three-fold symmetry axis of the crystal. Also, the x axis is selected so that it lies in a glide plane.

(Each glide plane contains the three-fold axis and a unit cell edge). The location of the x axis in this crystal had previously been determined by means of an X-ray precession photograph of the crystal (Spencer and Hughes, 1978). However, there is an ambiguity of 60° in the orientation of the x axis which is not resolved by the X-ray method. This ambiguity is removed by arbitrary selecting the (right handed) coordinate system xyz so that the unit cell edge which lies in the xz-plane extends from the origin into the second or fourth quadrants (rather than into the first and third quadrants). The orientation of this axis was found using NMR, by comparing the width of the ^{23}Na resonance line at the setting $\theta = 54.7^\circ$ and $\phi = 0^\circ$ and 60° . The second moment of the centre line in the frequency domain, due to the magnetic dipole-dipole interaction, is given by (Andrew et al., 1962).

$$S = \{29.57 - 2.97\cos 2\theta - 9.14\cos 4\theta + 6.04(2\sin 2\theta - \sin 4\theta)\cos 3\phi\} 10^4 \text{ Hz}^2 \quad (3.3)$$

relative to the crystal coordinate system defined above. At $\theta = 54.7^\circ$, the satellites overlap the centre line. However, the ϕ dependence of the second moment of the combined resonance line should still be of the same form as Eq. (3.3).

It can be seen from this equation that the dipolar second moment for $\theta = 54.7^\circ$ is a maximum at $\phi = 0^\circ$ and a minimum at $\phi = 60^\circ$. The FID which is the Fourier Transform

of the NMR signal in the frequency domain, should therefore be narrower in the time domain at $\phi = 0^\circ$ (and $\theta = 54.7^\circ$) than at $\phi = 60^\circ$. The ^{23}Na FID's in NaNO_3 obtained for $\theta = 54.7^\circ$ and $\phi = 0^\circ$ and 60° are shown in Fig. 3.8. The FID's were averaged eight times and then read out from the signal averager via the X-Y recorder. It is clear from the above discussion that the ϕ values associated with the two FID's are as shown in Fig. 3.8. This uniquely identifies the orientation of the x axis in our crystal.

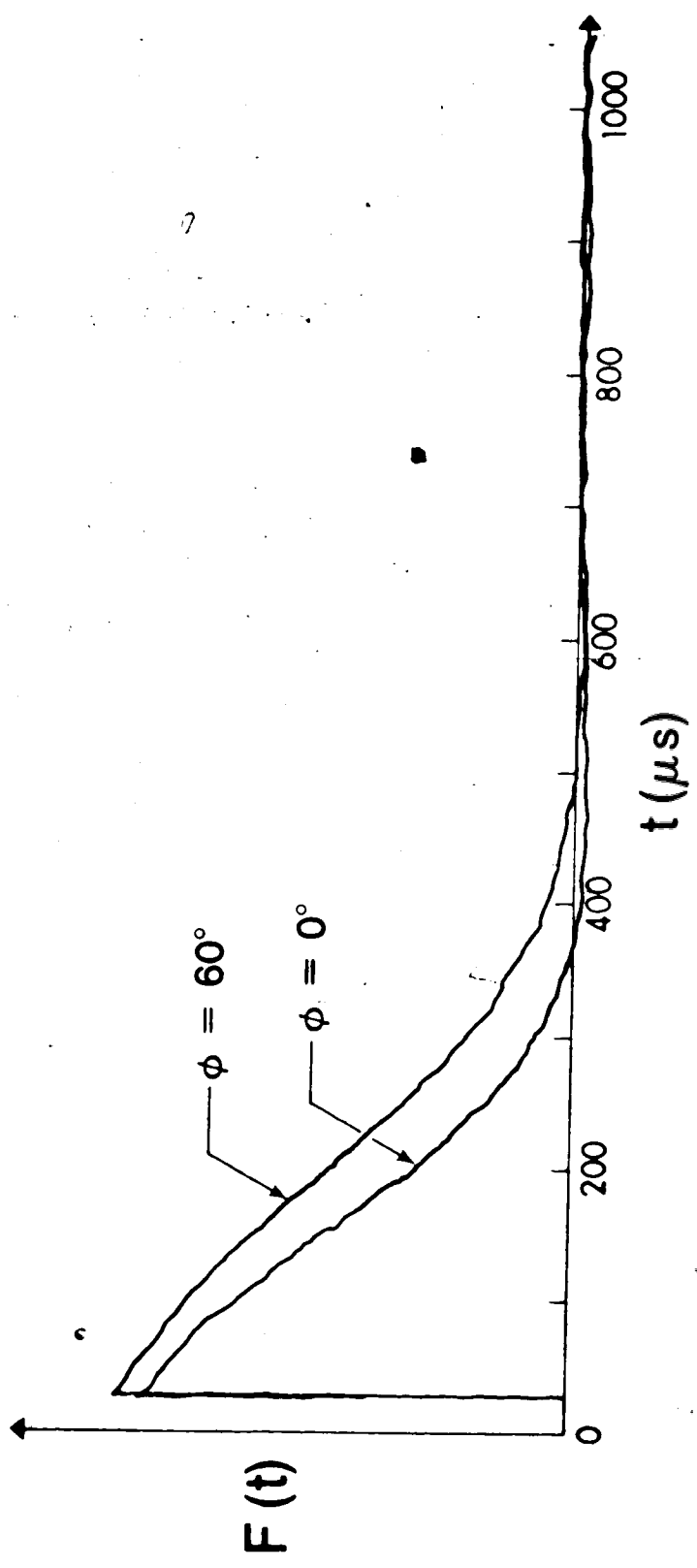
3.5.3 Measurement of T_1 of ^{23}Na in NaNO_3 .

The NaNO_3 crystal was oriented so that ϕ was equal to 30° by rotating the collar B about axis 2 (see Fig. 3.7). The angle θ was set at 54.7° , where resonance overlap occurs, by rotating the sample holder about axis 1. The position of best overlap was taken to be the orientation at which the FID was approximately Gaussian in shape. Rotation of the crystal through about 0.1° in either direction caused the FID to change shape significantly and in particular to overshoot because the satellites became off resonance. Thus, the setting of the crystal was very delicate.

The equipment was allowed to warm up for one hour before T_1 data were taken. Since the T_1 of ^{23}Na nuclei is approximately 6 seconds (Kasahara et al., 1977; Spencer and Hughes, 1978), a repetition rate of 34.5 seconds was

Figure 3.8

Free induction decay $F(t)$ of ^{23}Na in NaNO_3 at $\theta = 54.7^\circ$,
and $\phi = 0^\circ$ and 60° .



used. Also, eleven different τ values ranging from 0.1 to 15 seconds were used in random order. Otherwise the method was the same as for the NaCl crystal. In particular, each FID was averaged eight times. Data obtained in the fourth channel (32 μ s after the end of the 90° pulse) are shown in Fig. 3.9. As was the case for NaCl, T_1 values were also obtained from the data in the seventeenth, fifty-seven and ninety-seventh channels, and the weighted mean was calculated. The measurements were repeated, using the same τ values, with ϕ covering the range 0° to 120° in 15° steps. For reasons discussed in section 4, great care was taken to keep the operating conditions, and in particular the control settings on the rf phase-sensitive detector, the same for all ϕ values. The T_1 values are summarized in Table 2.

The temperature of the sample was 299K, as in the case of the NaCl crystal.

Figure 3.9

$M_O - M_Z$ versus pulse separation time τ for ^{23}Na in NaNO_3
at 299K and $\phi = 30^\circ$.

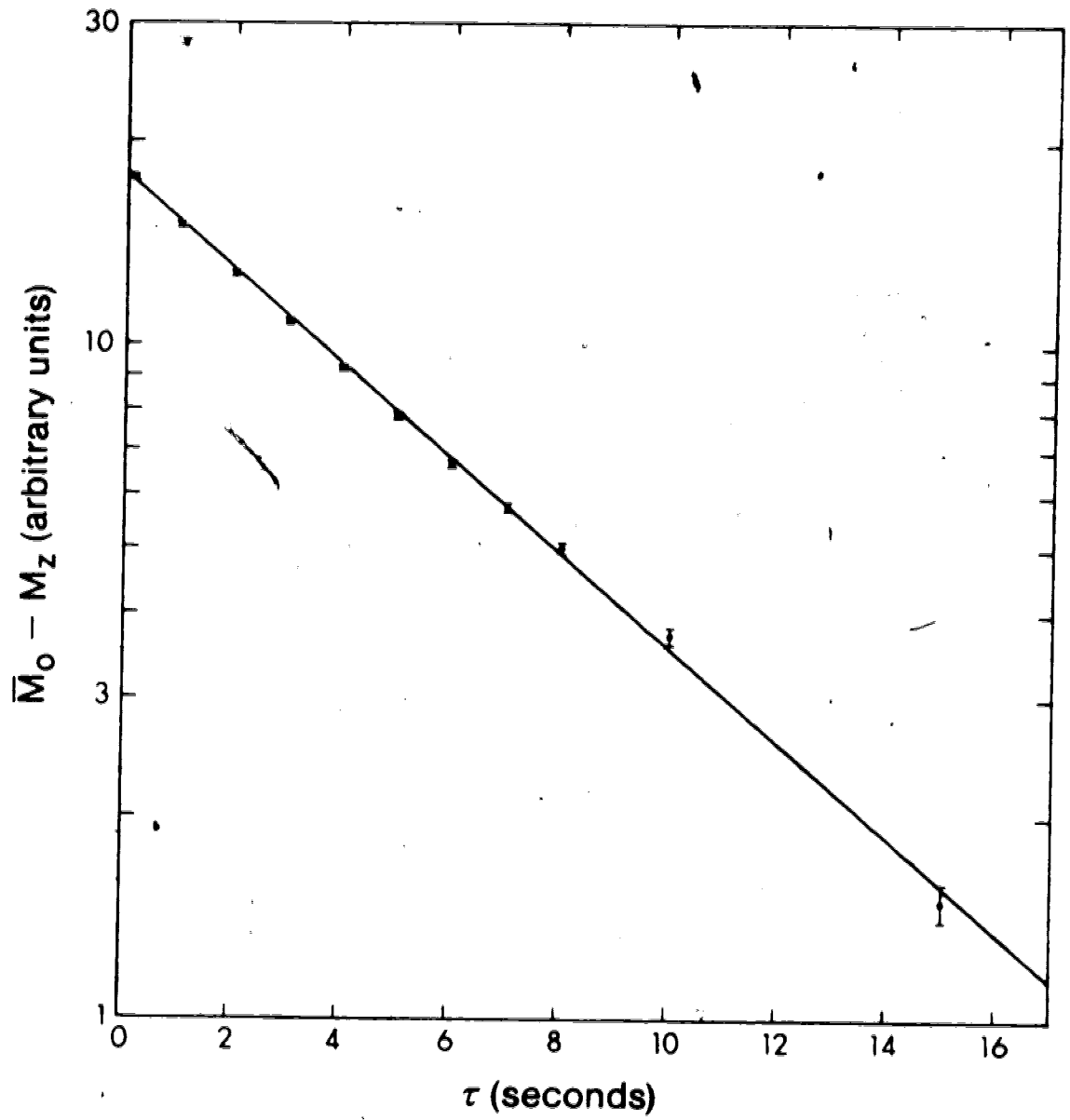


TABLE 2

T_1 of ^{23}Na in NaNO_3 at $\theta = 54.7^\circ$ and at various values of ϕ . The values in the second, third, fourth and fifth columns were obtained using data from different channels of the signal averager.

ϕ	T_1 (4th)	T_1 (17th)	T_1 (57th)	T_1 (97th)	Error (Scatter)	Error (Std.dev.)	Mean T_1
0	6.143 ± 0.040	6.135 ± 0.053	6.252 ± 0.052	6.328 ± 0.066	0.042	0.025	6.194 ± 0.042
15	6.138 ± 0.035	6.082 ± 0.041	6.171 ± 0.046	6.228 ± 0.038	0.031	0.020	6.155 ± 0.031
30	6.196 ± 0.060	6.139 ± 0.046	6.107 ± 0.043	6.172 ± 0.056	0.019	0.025	6.145 ± 0.025
45	6.166 ± 0.048	6.199 ± 0.040	6.214 ± 0.036	6.197 ± 0.041	0.009	0.020	6.197 ± 0.020
60	6.097 ± 0.047	6.233 ± 0.032	6.249 ± 0.051	6.405 ± 0.043	0.059	0.020	6.251 ± 0.059
75	6.262 ± 0.034	6.169 ± 0.024	6.240 ± 0.037	6.267 ± 0.040	0.025	0.016	6.218 ± 0.025
90	6.219 ± 0.053	6.244 ± 0.048	6.317 ± 0.056	6.227 ± 0.049	0.021	0.026	6.249 ± 0.026
105	6.173 ± 0.041	6.149 ± 0.044	6.231 ± 0.034	6.274 ± 0.056	0.025	0.021	6.203 ± 0.025
120	6.159 ± 0.044	6.074 ± 0.047	6.168 ± 0.059	6.192 ± 0.056	0.026	0.025	6.143 ± 0.026

CHAPTER 4

DISCUSSION

We found that T_1 of ^{23}Na in our single crystal of NaCl at room temperature (299K) was 14.60 ± 0.15 seconds, where the error limits include random errors but not necessarily all types of systematic errors. Other published values of T_1 for ^{23}Na in NaCl are 14.2 ± 0.5 seconds at 300K (Schumacher, 1958), 14.2 ± 0.5 seconds at 300K (Satoh, 1965), and 14.1 ± 0.2 seconds at 295K (Spencer and Hughes, 1978). (Satoh's value has been read off a graph. He did not explicitly state his error limits. However, it can be inferred that they were approximately ± 0.5 seconds.) The T_1 of NaCl is approximately inversely proportional to the square of the absolute temperature. Spencer and Hughes' value therefore corresponds to 13.75 ± 0.2 seconds at 299K. While our value agrees with values found by Schumacher and Satoh within the combined error limits, it does not agree with the value found by Spencer and Hughes (1978) using a cw technique. Satoh, and Spencer and Hughes, used a single crystal of NaCl, as we did in our measurements, so the discrepancy cannot be attributed to using a different type of sample. The reason for the discrepancy between our value and that of Spencer and Hughes is not known. However, the fact that our T_1 is longer than all the other published values raises the question whether there is a systematic error in our T_1 values, due to nonlinearity of the rf phase-sensitive

detector for example.

The T_1 of ^{23}Na in NaNO_3 at 299K, as measured in different channels (at different times after the 90° pulse), are shown for various of ϕ in Table 2. Values of T_1 , calculated from data obtained using different channels, are in quite good agreement with each other, except for $\phi = 60^\circ$ where there is a significant tendency for T_1 to increase with increasing channel number.

The resonance linewidth is a minimum at $\phi = 60^\circ$ (Andrew et al., 1962) (see also section 3.5.2). The resonance overlap achieved will therefore be less at this orientation than at any other. However, if this is the reason for the dependence of T_1 on channel number, one would expect almost the same trend at $\phi = 45^\circ$ and 75° , and there is little evidence of this in Table 2.

Another possible reason why the measured T_1 might depend upon the channel number is the presence of crystal imperfections. In an imperfect region of the crystal, the satellites will not overlap the centre line properly, and will not be coupled to it by spin exchanges. In that case, the centre line and satellites will relax independently of one another. This is shown mathematically by the following. In the case of a common spin temperature, the relaxation of the population differences N_1 between the $m = 3/2$ and $1/2$ levels, N_0 between the $m = 1/2$ and $-1/2$ levels and N_{-1} between the $m = -1/2$ and $-3/2$ levels following a 180° pulse at $t = 0$, is given by

$$N_{\pm 1} = N_0 = n_0 [1 - 2 \exp\{-2(W_1 + 4W_2)t/5\}], \quad (4.1)$$

where n_0 is the population difference between adjacent levels in thermal equilibrium. If there are no spin exchanges between the centre line and satellites, the relaxation following a 180° pulse is given by (cf. Andrew and Tunstall, 1961)

$$N_{\pm 1} = n_0 [1 - 2 \exp(-2W_2 t)] \quad (4.2)$$

$$N_0 = n_0 [1 + 2 \exp(-2W_1 t) - 4 \exp(-2W_2 t)]. \quad (4.3)$$

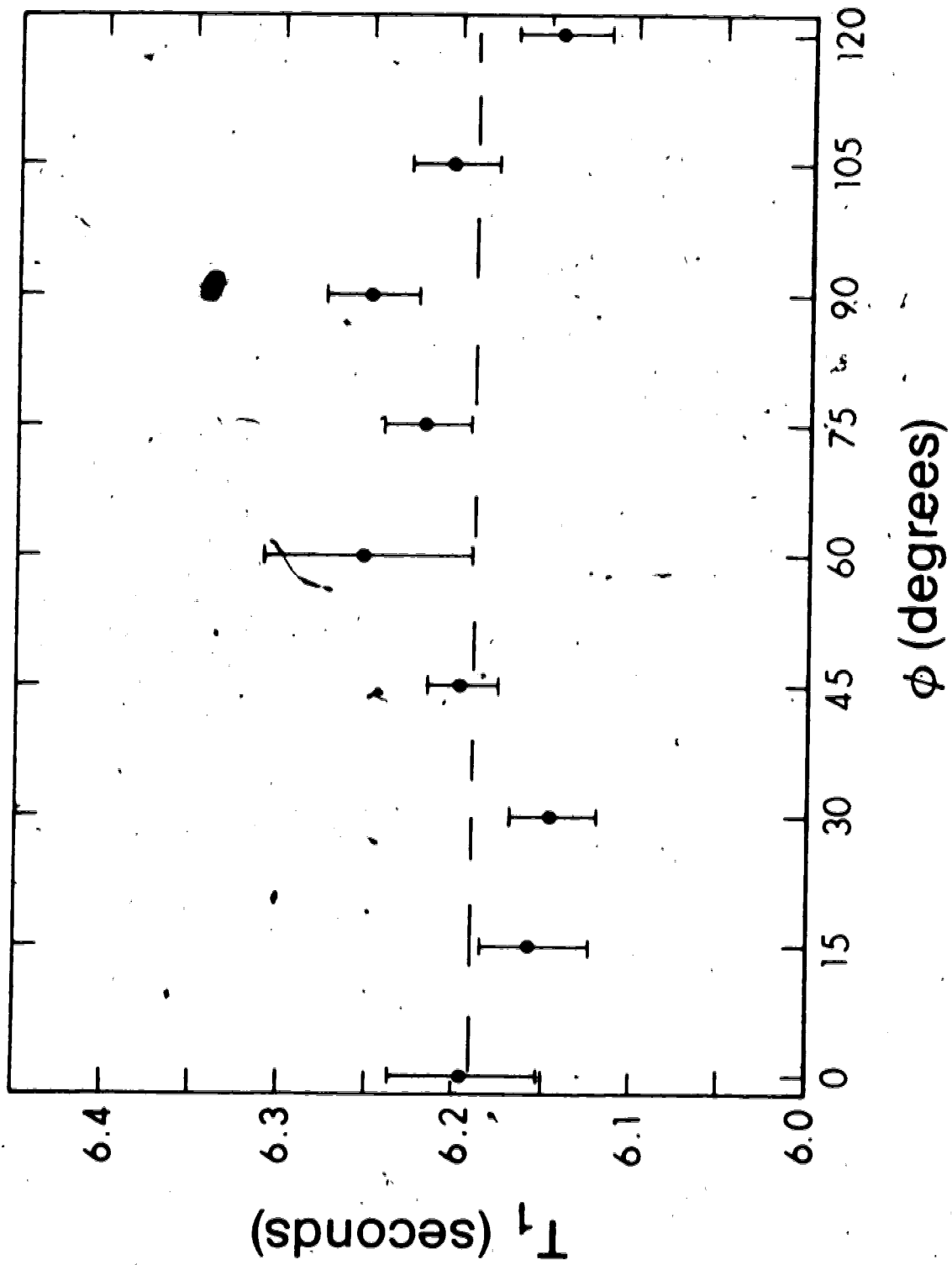
In imperfect regions of the crystal, the satellites will decay more rapidly than the centre line in the FID following a 90° pulse. Thus, the satellites will contribute less to the FID as time increases, i.e., as the channel number increases. Values of T_1 would then in general depend upon the channel number, though if W_1 and W_2 are equal, it can be seen from Eqs. (4.1), (4.2) and (4.3) that the relaxation is the same whether or not spin exchanges occur. It can be shown, using the M-tensor components found by Spencer and Hughes (1978), that at $\theta = 54.7^\circ$, W_2/W_1 for ^{23}Na in NaNO_3 varies between 0.967 at $\phi = 0^\circ$ and 1.178 at $\phi = 60^\circ$. Imperfections should thus have the largest effect on the measured T_1 values at $\phi = 60^\circ$. However, it has been shown (Hughes, 1981) that even if imperfections were such that the centre line alone was

observable in 10% of the volume of the crystal, the effect would be to reduce the T_1 measured at $\phi = 60^\circ$ by less than 1%. A rough comparison of the amplitude of the FID of the centre line only (at $\theta = 0^\circ$) with that of the combined satellites and centre line (at $\theta = 54.7^\circ$) showed that the volume of the crystal affected by imperfection is small. Thus, the dependence of T_1 upon channel number at $\phi = 60^\circ$ is unlikely to be due to crystal imperfections, and the reason for it is unknown.

The weighted mean values of T_1 given in the last column of Table 2 are shown as a function of ϕ in Fig. 4.1. The data look as if they vary as $-\sin 3\phi$. However, this is probably coincidental. When the error bars are taken into account, the data fit quite well to the dashed straight line drawn at the weighted mean value of $T_1 = 6.19$ seconds. Of the nine data points, only four differ from 6.19 seconds by much more than the error bar. Bearing in mind that the error bars represent 68% confidence limits, that is not too unreasonable, especially since it has been found in many laboratories that the day-to-day reproducibility of T_1 values measured by the pulse technique is not high. We therefore deduce that T_1 for ^{23}Na in NaNO_3 is independent of ϕ as predicted theoretically (Hughes and Spencer, 1979) (see also section 2.3). As will be mentioned later, there is evidence of a systematic error in our values of T_1 . However, the experimental conditions were kept the same for all values of ϕ . The systematic

Figure 4.1

T_1 of ^{23}Na in a single crystal of NaNO_3 at 299K, as a function of ϕ for $\theta = 54.7^\circ$. The error bars represent the larger of the two standard errors calculated by the least squares fit.



error should therefore not affect the form of the orientation dependence of T_1 .

Our T_1 value of 6.19 seconds for ^{23}Na in NaNO_3 at 299K can be compared with two other values. Using fitted parameters found by Kasahara et al. (1977), we find a T_1 value at 299K of 6.03 seconds. By substituting values of the M-tensor components found by Spencer and Hughes (1978) in Eq. (2.57), we find that the T_1 of ^{23}Na in NaNO_3 to be 6.42 ± 0.08 seconds at 295K. Correcting this value to 299K using the temperature dependence of T_1 found by Kasahara et al. (1977), we find that T_1 at 299K should be 6.23 ± 0.08 seconds. Our value of 6.19 seconds is in excellent agreement with the values deduced from Spencer and Hughes' work and from the measurements of Kasahara et al. There is no evidence of the kind of systematic discrepancy with T_1 of ^{23}Na in NaCl . However, as will become clear in the next paragraph, this excellent agreement is probably coincidental.

Finally, we consider possible defects in our equipment or procedure that might cause erroneous values of T_1 . The measurements reported in this thesis were obtained with a smaller reference signal (17% on the cw reference level meter) than that recommended in the manual of the rf phase-sensitive detector (50% on the cw reference level meter). This was because of a loss of signal in the phase shifter. Recently, measurements made by Pandey (1981) indicate that the use of a reference signal of the recommended amplitude

gives T_1 values which are roughly 2% larger than those reported in this thesis. Therefore, this cannot explain the fact that our measured value of T_1 for ^{23}Na in NaCl was longer than other published values. Pandey (1981) also found that use of the low-Q setting in the rf phase-sensitive detector, gave T_1 values approximately 3% larger than the values obtained with the high-Q setting used for the measurements reported in this thesis. Generally, quite good agreement is found between T_1 values measured on different days with the same control settings on the rf phase-sensitive detector. All this suggests that the rf phase-sensitive detector may not be perfectly linear, and that the nonlinearity varies with the control settings of the rf phase-sensitive detector. Some confirmation of this has been found by reevaluating the T_1 of ^{23}Na in NaNO_3 using the last six data points (those with $\tau \geq 5$ seconds, see Fig. 3.9). These T_1 values were 1% smaller on the average than those found by taking all eleven data points. This suggests that the equipment may indeed be nonlinear. In order to achieve good accuracy of say $\pm 1\%$ in T_1 values, our rf phase-sensitive detector may therefore need to be replaced by a better instrument.

BIBLIOGRAPHY

- Abragam, A., 1961, The Principles of Nuclear Magnetism
(Oxford: Clarendon Press).
- Abragam, A. and Proctor, W.G., 1958, Phys. Rev., 109, 1441.
- Andrew, E.R., 1955, Nuclear Magnetic Resonance (Cambridge:
University Press) p. 127.
- Andrew, E.R., Eades, R.G., Hennel, J.W. and Hughes, D.G.,
1962, Proc. Phys. Soc., 79, 954.
- Andrew, E.R. and Swanson, K.M., 1960, Proc. Phys. Soc., 75,
582.
- Andrew, E.R. and Tunstall, D.P., 1961, Proc. Phys. Soc.,
78, 1.
- Avogadro, A., Cavelius, E., Muller, D. and Petersson, J.,
1971, Phys. Status Solidi B, 44, 639.
- Becker, K.D., 1978, Phys. Stat. Sol: (b), 87, 589.
- Bersohn, R., 1952, J. Chem. Phys., 20, 1505.
- Bevington, P.R., 1969, Data Reduction and Error Analysis
for the Physical Sciences (New York: McGraw-Hill)
chapter 6.
- Birge, R.T., 1932, Phys. Rev., 40, 207.
- Bloembergen, N., Shapiro, S., Pershan, P.S. and Artman, J.
O., 1959, Phys. Rev., 114, 445.
- Bonera, G., Borsa, F. and Rigamonte, A., 1970, Phys. Rev.
B, 2, 2784.
- Buess, M.L. and Petersen, G.L., 1978, Rev. Sci. Instrum.,
49, 1151.
- Cohen, M.H. and Reif, F., 1957, Solid State Physics, Vol.

- 5, eds. F. Seitz and D. Turnbull (New York: Academic Press) p. 321.
- Hughes, D.G., 1973, *J. Phys. C*, 6, 3797.
- Hughes, D.G., 1981, Private communication.
- Hughes, D.G. and Reed, K., 1971, *J. Phys. C*, 4, 2945.
- Hughes, D.G. and Spencer, P.A., 1979, *J. Magn. Reson.*, 33, 221.
- Kasahara, M., Hikita, T., Tatsuzaki, I. and Sasakawa, K., 1977, *J. Phys. Soc. Japan*, 42, 1239.
- McLachlan, L.A., 1980, *J. Magn. Reson.*, 39, 11.
- Mieher, R.L., 1960, *Phys. Rev. Lett.*, 4, 57.
- Pandey, L., 1981, Private communication.
- Pietilä, A., 1968, *Ann. Acad. Sci. Fennicae*, A VI, No. 271.
- Pound, R.V., 1950, *Phys. Rev.*, 79, 685.
- Ramsey, N.F., 1953, *Nuclear Moments* (New York: Wiley).
- Sato, M., 1965, *J. Phys. Soc. Japan*, 20, 1008.
- Schumacher, R.T., 1958, *Phys. Rev.*, 112, 837.
- Slichter, C.P., 1963, *Principles of Magnetic Resonance*, (New York: Harper and Low).
- Snyder, R.E. and Hughes, D.G., 1971, *J. Phys. C*, 4, 227.
- Spencer, P.A. and Hughes, D.G., 1978, *J. Phys. C*, 11, 183.
- Squires, G.L., 1976, *Practical Physics* (London: McGraw-Hill) p. 43.
- Van Kranendonk, J., 1954, *Physica*, 20, 781.
- Van Kranendonk, J. and Walker, M., 1967, *Phys. Rev. Lett.*, 18, 701.

- Van Kranendonk, J. and Walker, M., 1968, Can. J. Phys.,
46, 2241.
- Van Vleck, J.H., 1948, Phys. Rev., 74, 1168.
- Weber, M.J., 1963, Phys. Rev., 130, 1.
- Wikner, E.G., Blumberg, W.E. and Hahn, E.L., 1960, Phys.
Rev. 118, 631.
- Yosida, K. and Moriya, T., 1956, J. Phys. Soc. Japan, 11,
33.
- Zak, J., 1964, Physica, 30, 401.

APPENDIX 1

Weighted least squares fit to a straight line and the error in the fitted parameters.

We suppose that n data points $x_1y_1, x_2y_2, \dots, x_ny_n$, are to be fitted to the straight line

$$y = mx + c. \quad (\text{A1.1})$$

We suppose that the individual points have associated (relative) weighting factors w_1, w_2, \dots, w_n . According to Squires (1976), the best value of the slope m is given by

$$m = \frac{\sum w_i (x_i - \bar{x}) y_i}{D_w} \quad (\text{A1.2})$$

where

$$D_w = \sum w_i (x_i - \bar{x})^2. \quad (\text{A1.3})$$

Since the mean value \bar{x} is only available after all the data have been inserted and the fit has been completed, it is more convenient to express \bar{x} in terms of summations as follows:

$$\bar{x} = \frac{\sum w_i x_i}{\sum w_i} \quad (\text{A1.4})$$

It follows that

$$D_w = \sum w_i x_i^2 - \frac{(\sum w_i x_i)^2}{\sum w_i}. \quad (\text{A1.5})$$

Substituting in Eq. (A1.2), we find that

$$m = \frac{\sum w_i \sum w_i x_i y_i - \sum w_i x_i \sum w_i y_i}{\sum w_i \sum w_i x_i^2 - (\sum w_i x_i)^2} \quad (\text{A1.6})$$

This expression agrees with Eq. (6-12) given by

Bevington (1969), provided w_i is replaced by $1/\sigma_i^2$

where σ_i is the standard error of the i th data point.

Similarly, we find that the best value of c is

given by

$$c = \bar{y} - m\bar{x} \quad (\text{A1.7})$$

or

$$c = \frac{\sum w_i y_i \sum w_i x_i^2 - \sum w_i x_i \sum w_i x_i y_i}{\sum w_i \sum w_i x_i^2 - (\sum w_i x_i)^2} \quad (\text{A1.8})$$

The standard error in m and c , as determined from the standard error of each data point, is given by (Bevington, 1969)

$$\alpha_m = \left\{ \frac{\sum \sigma_i^{-2}}{[\sum \sigma_i^{-2} \sum (x_i/\sigma_i)^2 - (\sum x_i/\sigma_i^2)^2]} \right\}^{\frac{1}{2}} \quad (\text{A1.9})$$

and

$$\alpha_c = \left\{ \frac{(\sum x_i/\sigma_i)^2}{[\sum \sigma_i^{-2} \sum (x_i/\sigma_i)^2 - (\sum x_i/\sigma_i^2)^2]} \right\}^{\frac{1}{2}} \quad (\text{A1.10})$$

An equally good, or perhaps better, estimate of the error is provided by the scatter of the data about the straight line. The standard error in m and c , as determined by the scatter, is given by (Squires, 1976)

$$\alpha_m = \left\{ \frac{\sum w_i d_i^2}{(n-2) \sum w_i (x_i - \bar{x})^2} \right\}^{\frac{1}{2}} \quad (\text{A1.11})$$

and

$$\alpha_c = \left\{ \left[\frac{1}{\sum w_i} + \bar{x}^2 / \sum w_i (x_i - \bar{x})^2 \right] \frac{\sum w_i d_i^2}{(n-2)} \right\}^{\frac{1}{2}} \quad (\text{A1.12})$$

where

$$d_i = y_i - mx_i - c \quad (\text{A1.13})$$

is the deviation of the i th data point (in the y direction) from the straight line. Substituting for \bar{x} and d_i using Eqs. (A1.4) and (A1.13) we can express α_m and α_c in terms of summations as follows:

$$\alpha_m = \left\{ \frac{\sum w_i (w_i y_i^2 + c^2 \sum w_i - m^2 \sum w_i x_i^2 - 2c \sum w_i y_i)}{(n-2) (\sum w_i \sum w_i x_i^2 - (\sum w_i x_i)^2)} \right\}^{\frac{1}{2}} \quad (\text{A1.14})$$

and

$$\alpha_c = \left\{ \frac{(\sum w_i x_i^2) (\sum w_i y_i^2 + c^2 \sum w_i - m^2 \sum w_i x_i^2 - 2c \sum w_i y_i)}{(n-2) [\sum w_i \sum w_i x_i^2 - (\sum w_i x_i)^2]} \right\}^{\frac{1}{2}} \quad (\text{A1.15})$$

We have not found these expressions (A1.14) and (A1.15) in the literature. However, they are very useful for calculating the standard error in the fitted parameter m and c by means of a programmable calculator, since the data need only be retained in the form of summations.

(The only disadvantage of using Eqs. (A1.14) and (A1.15) is that large numbers of nearly equal magnitude are subtracted. Care must therefore be taken to use enough significant figures in the calculation.)

APPENDIX 2

Method of obtaining the standard deviations and weighting factors needed in our least squares fitting procedure.

Experimentally we found that the standard deviation caused by random error in M_z is independent of τ and is therefore the same as that associated with M_o . This standard deviation, $\sigma[M_o]$, was calculated from the scatter of the values of M_o . Also, the mean value of M_o , say \bar{M}_o , was used in calculating values of $\ln(M_o - M_z)$. The standard deviation of $\ln(\bar{M}_o - M_z)$ is given by

$$\sigma[\ln(\bar{M}_o - M_z)] = \sigma[\bar{M}_o - M_z] / (\bar{M}_o - M_z). \quad (A2.1)$$

If we assume that the errors in \bar{M}_o and M_z are uncorrelated, then the standard deviation of $\ln(\bar{M}_o - M_z)$ will be given by

$$\sigma[\ln(\bar{M}_o - M_z)] = \{(\sigma[\bar{M}_o])^2 + (\sigma[M_z])^2\}^{1/2} / (\bar{M}_o - M_z). \quad (A2.2)$$

The standard deviation in M_z , viz. $\sigma[M_z]$, is equal to the $\sigma[M_o]$ obtained previously. The standard deviation of \bar{M}_o , viz. $\sigma[\bar{M}_o]$ is given by $\sigma[M_o] / \sqrt{n}$, where n is the number of individual values of M_o used to calculate \bar{M}_o . (For our measurements of T_1 of ^{23}Na in a single crystal of NaNO_3 , n was 12.) Thus, the standard deviation in $\ln(\bar{M}_o - M_z)$ is

$$\sigma[\ln(\bar{M}_o - M_z)] = \sigma[M_o] \{1 + (1/n)\}^{1/2} / (\bar{M}_o - M_z). \quad (A2.3)$$

The weighting factor associated with each data point is inversely proportional to the square of the standard deviation. Thus, the weighting factor associated with the i th data point is given by

$$w_i = (\bar{M}_O - M_Z)^2 / (\sigma[M_O])^2 \{1 + (1/n)\}. \quad (A2.4)$$

We obtain the value of T_1 by performing a least squares fit of $\ln(\bar{M}_O - M_Z)$ versus τ , and finding T_1 from the slope of the best straight line using Eq. (A1.6). The error in T_1 is found using Eqs. (A1.9) and (A1.14). We manually calculate the standard deviation of $(\bar{M}_O - M_Z)$ which is given by the numerator on the right hand side of Eq. (A2.3). This quantity, which is the same for all data points, is then fed to a programmable calculator which performs the least squares fit. The program evaluates $\sigma[\ln(\bar{M}_O - M_Z)]$ for each data point by means of Eq. (A2.3). It then takes the inverse square of these quantities and uses them as the weighting factors in evaluating the summations which occur in Eqs. (A1.6), (A1.9) and (A1.14). The standard deviation σ_1 which appears in Eq. (A1.9) is of course $\sigma[\ln(\bar{M}_O - M_Z)]$, and this has already been calculated.

The program used to calculate T_1 is described in Appendix 3.

APPENDIX 3

Program for calculating T_1 from values of $(\bar{M}_O - M_Z)$ and τ .

It can be seen from Eqs. (2.19) and (A1.1) that $T_1 = -1/m$. Also, α_{T_1} the standard error in T_1 , is given by $\alpha_{T_1} = \alpha_m/m^2$. Two estimates of α_{T_1} are obtained, corresponding to the two different estimates of α_m given by Eqs. (A1.9) and (A1.14). For convenience in plotting the data graphically, the program also computes c , the intercept of the straight line, and the corresponding value of $(\bar{M}_O - M_Z)$. It also calculates the value of τ for which $(\bar{M}_O - M_Z)$ is reduced by exactly a factor of 10.

The following summations are accumulated in the registers indicated:

$\sum w_i$	Reg. 0
$\sum w_i x_i$	Reg. 1
$\sum w_i x_i^2$	Reg. 2
$\sum w_i y_i$ (where $y_i = \ln(M_O - M_Z)_i$)	Reg. 3
$\sum w_i x_i y_i$	Reg. 4
$\sum w_i y_i^2$	Reg. 5

The standard deviation $\sigma[\bar{M}_O - M_Z]$, which has previously been manually determined, is stored in Reg. 9.

The program, which was developed by my supervisor for the HP.67 programmable calculator, is as follows:

LBL A	CLR REG	FIX SCI	DSP 3
RTN	LBL B	STO 8	$x \neq y$
STO 7	$x \neq y$	RCL 9	\div
x^2	STO 6	STO+0	x
STO+1	RCL 7	x	STO+2
RCL 6	RCL 8	ln	x
STO+3	ENTER	ENTER	RCL 7
x	STO+4	+	RCL 8
ln	x	STO+5	ISZ
RTN	LBL C	RCL 0	RCL 4
x	RCL 1	RCL 3	x
-	RCL 0	RCL 2	x
RCL 1	x^2	-	STO 6
\div	STO 9	1/x	CHS
STO A	RCL 3	RCL 2	x
RCL 1	RCL 4	x	-
RCL 6	\div	STO 8	e^x
STO D	RCL 5	RCL 8	x^2
RCL 0	x	+	RCL 9
x^2	RCL 2	x	-
RCL 8	RCL 3	x	2
x	-	RCL 0	x
RCL	2	-	RCL 6
x	\div	$\sqrt{\quad}$	STO 7
RCL 9	x^2	\div	STO B
RCL 0	RCL 6	\div	$\sqrt{\quad}$

STO 6

RCL 9

 x^2

÷

STO C

RCL A

1

0

ln

x

STO E

RTN

To obtain the value of T_1 , the program is first loaded. Then the A key is pressed. This clears the registers in preparation for the calculation and sets the correct display. At this point, the value of $\sigma[\bar{M}_O - M_Z]$ is inserted in Reg. 9. The first value of τ is entered, followed by the ENTER key. This is followed by the first value of $(M_O - M_Z)$. The B key is then pressed and this evaluates the summations associated with the first data point. The second value of τ is then entered, followed by the ENTER key, the second value of $(M_O - M_Z)$, and the B key in that order. The process is repeated for all the other data, at which point the summations in Regs. 0 to 5 are complete. Key C is pressed, and this causes the value of T_1 to be computed and presented in Reg. A. The external error in T_1 (error due to the scatter of the data points) is presented in Reg. B. The internal error in T_1 (error associated with the standard deviation of each value of $\ln(\bar{M}_O - M_Z)$) is given in Reg. C. The best value of $\bar{M}_O - M_Z$ at $\tau = 0$ is given in Reg. D, and the value of τ at which $(\bar{M}_O - M_Z)$ has fallen by a factor of ten is given in Reg. E.